Random sequential adsorption of Pickering particles onto spherical emulsion droplet surfaces

Random sequential adsorption of Pickering particles onto spherical emulsion droplet surfaces.

Yi Feng, Giulia Del Duca, Antonio Buffo, and Elena Simone*

Department of Applied Science and Technology,

Politecnico di Torino, Torino, Italy.

(Dated: November 7, 2025)

Abstract

Pickering emulsions are attracting growing attention as carriers of active ingredients or micronutrients in pharmaceutical and food applications, due to their high stability and low toxicity. The adsorption process of Pickering particles significantly affects emulsion properties and can be described using the random sequential adsorption (RSA) approach. While most studies focus on small, amorphous, spherical particles, the common use of elongated, crystalline, micron-sized particles in Pickering emulsions makes it necessary to consider the curvature and finite size of emulsion droplet surfaces to correctly understand and predict the interfacial adsorption behavior. The present study employs a Monte Carlo (MC) method to simulate the RSA process of both spherical and elongated micron-sized particles. Key factors such as particle polydispersity, emulsion droplet–particle size ratio, contact angle, and particle number are investigated. From the MC simulations, a new expression for the available surface function, $ASF(\phi)$, with coverage-dependent exponent is proposed. Based on this, generalized coverage evolution models are established using response surface methodology to relate RSA conditions to $ASF(\phi)$ parameters. For spherical particles, jamming coverage and desorption energy under various conditions are reported. For capsule-shaped particles, an aspect ratio of $\epsilon = 2$ is found to yield higher coverage and faster adsorption. The proposed $ASF(\phi)$ expression outperforms existing fixed-exponent expressions. The generalized coverage evolution models show good agreement with MC testing simulations. The mean absolute percentage errors are less than 2.63% for spherical particles and 6.58% for elongated ones in the validation cases.

I. INTRODUCTION

Emulsions are widely used in pharmaceutical applications to protect active pharmaceutical ingredients (API) and to control their release [1]. Pickering emulsions, which are stabilized by solid particles, are attractive in pharmaceutical applications due to their high stability and low toxicity [2]. The properties of Pickering emulsions are closely linked to the adsorption process of the stabilizing particles, characterized by the coverage, ϕ, defined as the fraction of the droplet surface area occupied by adsorbed particles. The low-coverage

* Contact author: elena.simone@polito.it

behaviors of this adsorption process affect the size distribution of the emulsion droplets. The adsorbed particles stabilize the droplets, preserving the emulsion microstructure from coalescence and breakage. A faster adsorption process may lead to smaller droplets in a coalescence-dominated preparation process, but larger ones in a breakage-dominated process [3, 4]. Additionally, the asymptotic behaviors, which are the behaviors near the jamming state where no more particles can be adsorbed at the interface, affect the emulsion stability and eventually the API release rate. A higher jamming coverage, ϕ_{j}, increases the total desorption free energy of the Pickering particles, and thus enhances the stability of Pickering emulsions [5]. Regarding the release of the API, it is a diffusion process that depends on the size and particle coverage of emulsion droplets. Therefore, a thorough understanding of the adsorption process from both low-coverage and asymptotic perspectives is essential to design Pickering emulsions with desired microstructural properties for encapsulation and controlled release of APIs.

Depending on their physicochemical properties, Pickering particles may experience the short-range attraction and long-range repulsion [6]. As a result, the particles adsorbed at the interface of emulsion droplets can organize into various packing structures, including ordered arrangements [7], disordered arrangements [8, 9], or a combination of both [10]. In our previous experiments [11], curcumin crystals were used to stabilize water-in-oil Pickering emulsions. A disordered arrangement of elongated particles was observed on the droplet surfaces, as shown in FIG. 1, which can be attributed to the isotropic curvature of spherical emulsion droplets [12]. This study focuses on such disordered particle packings, which can be modeled using the random sequential adsorption (RSA) approach [13]. In the RSA model, particles arrive sequentially and attempt to adsorb at random locations on the surface [14]. A particle is adsorbed only if it does not overlap with any previously adsorbed particles, and once adsorbed, it remains fixed in place.

The RSA problem has been extensively investigated in the literature. When particles are small enough compared to the droplet, the adsorbing interfaces can be regarded as planes [5]. Consequently, particles can be simplified to two-dimensional (2D) shapes, while adsorbing surfaces can be simplified to a sufficiently large planar area with periodic boundary conditions [15]. Based on this simplification, the RSA of particles with various shapes has been studied, including discs [16], squares [14], rectangles [17], discorectangles [18], ellipses [18, 19], polygons [20], rounded polygons [21], and other irregular shapes [22]. Different

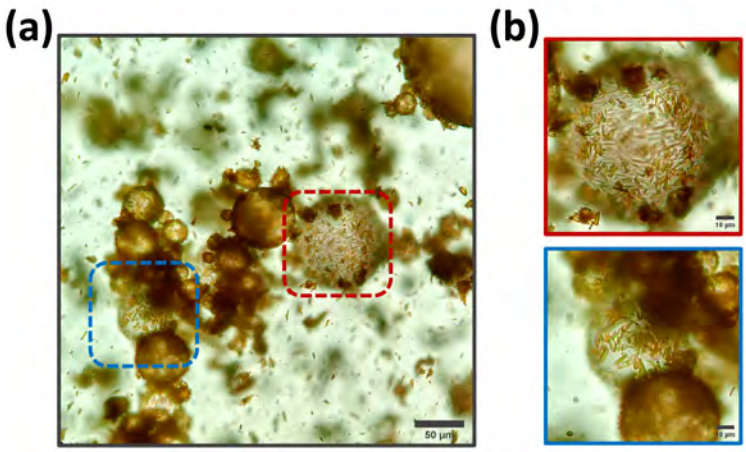

FIG. 1. Optical microscopy image of (a) water-in-oil emulsion droplets stabilized by elongated curcumin crystals, and (b) zoomed-in views showing the disordered arrangement of the crystals at the droplet interfaces. Brightness and contrast of the image were adjusted using Fiji software.

particle shapes typically result in varying jamming coverages and patterns.

Besides particle shape, other factors influencing the RSA process have been investigated. For particles with anisotropic shapes, their orientations and aspect ratios significantly affect both the low-coverage and asymptotic behaviors [23, 24]. For example, Ref. [25] found that the jamming coverage of aligned discorectangle particles gradually increases with the aspect ratio ϵ to a maximum value of $\phi_{\mathrm{j}} = 0.5589$. Meanwhile, the jamming coverage of unoriented particles first increases and then decreases with ϵ. A maximum $\phi_{\mathrm{j}} = 0.583 \pm 0.004$ was found at $\epsilon = 1.46$. Moreover, as polydisperse Pickering particles are widely adopted in industry, the effect of particle polydispersity on the RSA process has been explored in the literature. Particles with binary [26], uniform [27], power-law [28], and Gaussian [29] size distributions were investigated. Polydispersity was found to increase the jamming coverage because it introduces smaller particles that can occupy the spaces among the larger previously adsorbed ones [30].

The asymptotic and low-coverage behaviors are central topics in the RSA problem. The asymptotic behaviors have been found to follow a power law given by:

$$\phi_{\mathrm{j}} - \phi(n) \sim n^{-1/d}, \tag{1}$$

where ϕ_{j} is the jamming coverage, $\phi(n)$ is the coverage after n attempts of particle adsorption, d is a constant that depends on the shape and orientation of particles. Eq. (1) holds in the

vicinity of the jamming state, i.e., at a large n. Ref. [14] reported $d = 2$ for disks and Ref. [31] found $d = 3$ for anisotropic shapes. Consequently, Eq. (1) can be used to estimate ϕ_j by extrapolating the results of experiments or simulations [13, 32].

In addition to the extrapolation method, the jamming coverage can be obtained using the concept of an exclusion zone. The exclusion zone of an adsorbed particle is the area in which no other particle can be placed because it overlaps with the adsorbed one [32, 33]. The area available for adsorption is tracked by recording changes in exclusion zones. Particles are continuously adsorbed to the available area until no available area is left, namely, the jamming state. Ref. [34] divided the adsorbing surface into voxels and used them to approximate the available area. They obtained the jamming coverages of different polygons. Ref. [35] and Ref. [18] adopted the voxel method with a different criterion from that of Ref. [34] to exclude unavailable voxels. They obtained the jamming coverages of rectangles, discorectangles, and ellipses.

For the low-coverage behaviors, the key quantity is the coverage change rate, $\mathrm{d}\phi/\mathrm{d}t$. Ref. [36] related $\mathrm{d}\phi/\mathrm{d}t$ to the available surface function ($ASF(\phi)$), which represents the probability of successful adsorption at coverage ϕ. They derived an exact expansion for $ASF(\phi)$ based on geometric and statistical considerations for the RSA of disks on a plane, and achieved good accuracy with the first several terms. Ref. [37, 38] developed an analogous approach for the lattice RSA, while Ref. [39] extended this method to anisotropic particles, and proposed two polynomial expressions for $ASF(\phi)$. Ref. [40] modified the polynomials for $ASF(\phi)$ to make it consistent with Eq. (1). Ref. [41] adopted a fourth-order polynomial to fit their numerical results. Ref. [42] coupled $ASF(\phi)$ with diffusion, particle-wall interactions, and external forces and proposed a generalized coverage evolution model. Moreover, $\mathrm{d}\phi/\mathrm{d}t$ expressed using t and $(\phi_\mathrm{j} - \phi(t))$ with different exponents have been proposed [43–45].

The above studies provide valuable insights into the adsorption process of Pickering particles and are of great importance for the production of Pickering emulsions. It should be noted that most of these studies simplify the RSA process to two dimensions and neglect the effects of the curvature and the finite size of emulsion droplet surfaces. Such simplifications are reasonable for particles of sufficiently small sizes, such as those in the nanometer range. However, crystalline microparticles have received increasing attention for emulsion stabilization [46]. Micron-sized, crystalline particles obtained by milling or shearing starches and cellulose [47] are widely adopted due to their high availability and low cost. Alternatively,

polyphenol crystals can be used as Pickering particles due to their added health effects; as an example, our previous work has demonstrated the use of curcumin crystals as Pickering stabilizers of water-in-oil emulsions [11]. These larger particles lead to smaller emulsion droplet–particle size ratios, ranging from 10 to 100 [3, 48–52]. Under such conditions, the curvature and finite size of spherical droplet surfaces cannot be ignored. Despite their relevance, studies on the RSA of particles on curved surfaces remain limited [53–56].

To address these current gaps in knowledge, this study has two complementary aims: the first is to quantify the RSA behaviors (both low-coverage and asymptotic) of micron-sized spherical and capsule-shaped particles on the curved, finite emulsion droplet surfaces; and the second is to to present a research framework for developing a generalized coverage evolution model to efficiently predict the RSA process across varied conditions. Therefore, a Monte Carlo method accounting for the curvature and finite-size effects is developed to simulate the RSA process of both spherical and elongated (capsule-shaped) particles. Various influencing factors, such as particle polydispersity and average particle size, are explored. Particularly, based on the work of Ref. [18] and Ref. [35], we extend the voxel method to polydisperse spherical particles to accurately estimate their jamming coverage. With the MC results, the available surface function $ASF(\phi)$ can be evaluated. We then propose a new expression for $ASF(\phi)$ with a coverage-dependent exponent to better capture the adsorption process and compare it with fixed-exponent forms [39]. Finally, response surface methodology (RSM) is used to relate the fitted $ASF(\phi)$ parameters to the influencing factors, yielding a generalized coverage evolution model that predicts coverage evolution over diverse conditions without the need to run costly MC simulations. The novelty of this work lies in explicitly treating curvature and finite-surface effects of emulsion droplet surfaces and the RSM-based generalized coverage evolution model for RSA process.

The resulting jamming coverage data for spherical particles are directly relevant to modeling API release from Pickering emulsions. In addition, the generalized coverage evolution model provides a practical tool for predicting the RSA process across varied conditions, aiding the design and production of emulsions stabilized by micron-sized crystals.

The manuscript is organized as follows: Section II introduces the geometric relationships between Pickering particles and spherical emulsion droplet surfaces, the MC method used for the RSA process, and the generalized coverage evolution model. Section III focuses on the RSA process and the corresponding generalized coverage evolution model for spherical

particles, while Section IV addresses those for capsule-shaped particles. Conclusions are drawn in Section V.

II. METHODOLOGY

A. Geometric relationships

When the emulsion droplet–particle size ratio is small or moderate, such as between 10 to 100, the curvature and finite size of the emulsion droplet surface cannot be neglected. These effects can be incorporated by considering the geometric relationships between particles and droplets.

1. Spherical particles

The curvature of a spherical droplet surface influences the relative position of adsorbed particles through the contact angle. FIG. 2(a) shows the geometric relationships between a spherical particle and a spherical droplet. The emulsion droplet–particle center distance, l_{dp}, is determined by the radius of both the droplet and particle, r_{d} and r_{p}, and the contact angle, θ, as described by the following equation [57, 58]:

$$l_{\mathrm{dp}} = r_{\mathrm{d}} \cos\beta - r_{\mathrm{p}} \cos(\beta + \theta), \tag{2}$$

where $\theta \in [0,\, \pi]$, and the half-apex angle of the droplet cap, β, is calculated as:

$$\beta = \arctan\left(\frac{r_{\mathrm{p}}/r_{\mathrm{d}} \sin\theta}{1 - r_{\mathrm{p}}/r_{\mathrm{d}} \cos\theta}\right). \tag{3}$$

As shown in Fig. 2(a), β also represents the angle between γ_{ow} and a horizontal reference plane (a flat surface simplifying the spherical droplet surface as illustrated by the dashed line). Therefore, β measures the effect of the droplet surface curvature. For a fixed contact angle, β approaches zero when the emulsion droplet–particle radius ratio approaches infinity, $r_{\mathrm{d}}/r_{\mathrm{p}} \to \infty$, namely, the spherical droplet surface can be approximated by a plane when particles are sufficiently small [5]. When $r_{\mathrm{d}}/r_{\mathrm{p}}$ is small or moderate (i.e., between 10 and 100), the increased β makes it necessary to consider the effect of curvature.

The coverage of a single spherical particle, $\phi_{\mathrm{p,shp}}$, can be calculated as [53]:

$$\phi_{\mathrm{p,shp}} = \sin^2\left(\frac{\beta}{2}\right). \tag{4}$$

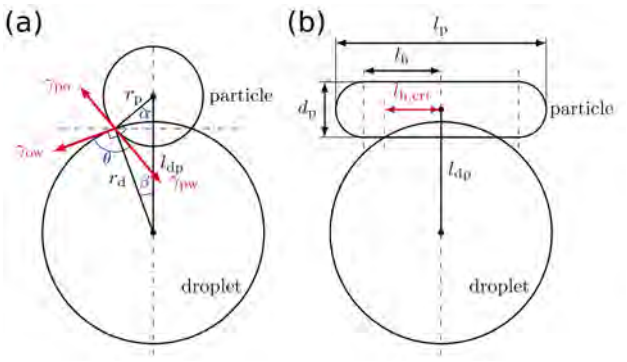

FIG. 2. Geometric relationship between (a) spherical particle and (b) capsule-shaped particle and a spherical droplet. γ_{po}, γ_{pw}, and γ_{ow} are surface tensions. This is a water-in-oil emulsion.

For polydisperse particles, the jamming coverage can be calculated as $\phi_{\mathrm{j}} = \sum_{i=1}^{N_{\mathrm{ad,j}}} \sin^2(\beta_i/2)$, where $N_{\mathrm{ad,j}}$ is the number of adsorbed particles at the jamming state.

Additionally, the free energy of particle desorption at the jamming state, ΔG_{d}, measures the stability of the Pickering emulsions [5]. A higher ΔG_{d} implies that the adsorbed particles require more energy to desorb from the emulsion droplets, and thus the Pickering emulsions are more stable. For the spherical particles and droplets, ΔG_{d} can be calculated as [5, 57]:

$$\Delta G_{\mathrm{d}} = \begin{cases} \gamma_{\mathrm{ow}}(A_{\mathrm{c}} - A_{\mathrm{po}}\cos\theta), & 0^\circ \le \theta < 90^\circ \\ \gamma_{\mathrm{ow}}(A_{\mathrm{c}} + A_{\mathrm{pw}}\cos\theta), & 90^\circ \le \theta \le 180^\circ \end{cases}, \tag{5}$$

where $A_{\mathrm{c}} = 4\pi r_{\mathrm{d}}^2 \phi_{\mathrm{j}}$ is the area of the oil-water interface occupied by the adsorbed particles, $A_{\mathrm{po}} = \sum_{i=1}^{N_{\mathrm{ad,j}}} 4\pi r_{\mathrm{p},i}^2 (1 - \sin^2(\alpha_i/2))$ is the total area of particle-oil interface, $A_{\mathrm{pw}} = \sum_{i=1}^{N_{\mathrm{ad,j}}} 4\pi r_{\mathrm{p},i}^2 \sin^2(\alpha_i/2)$ is the total area of particle-water interface, and $\alpha_i = \pi - \theta - \beta_i$ is the half-apex angle of the particle cap. In the following sections, ΔG_{d} is normalized by the thermal energy $k_{\mathrm{B}}T$, where k_{B} is the Boltzmann constant and $T = 298.15$ K is the temperature.

2. Capsule-shaped particles

Capsule-shaped particles are characterized by their aspect ratio, ϵ, defined as $\epsilon = l_{\mathrm{p}}/d_{\mathrm{p}}$, where l_{p} is the particle length and d_{p} is the diameter, as shown in FIG. 2(b). The contact area between capsule-shaped particles and spherical droplets can be complex, as the droplet surface may deform to satisfy the contact angle along the entire contact line [59, 60]. In

this study, however, the droplet surface is assumed to remain undeformed and perfectly spherical upon adsorption. The contact angle is assumed to be satisfied only at the central cross-section of the particle. Under this assumption, the emulsion droplet–particle center distance, l_{dp}, is calculated in the same manner as described in Section II A 1. The half length of the cylindrical part can be defined as:

$$l_{\mathrm{h}} = \frac{l_{\mathrm{p}} - d_{\mathrm{p}}}{2}. \tag{6}$$

Then, there is a critical value, $l_{\mathrm{h,crt}}$, equal to:

$$l_{\mathrm{h,crt}} = \sqrt{r_{\mathrm{d}}^2 - \left(l_{\mathrm{dp}} - r_{\mathrm{p}}\right)^2}, \tag{7}$$

so that if $l_{\mathrm{h}} \geq l_{\mathrm{h,crt}}$, the semi-spherical parts are completely outside the droplet, and if $l_{\mathrm{h}} < l_{\mathrm{h,crt}}$, the semi-spherical parts are partially inside the droplet. The corresponding critical aspect ratio can be calculated as $\epsilon_{\mathrm{crt}} = (2l_{\mathrm{h,crt}} + d_{\mathrm{p}})/d_{\mathrm{p}}$.

The coverage of a single capsule-shaped particle, $\phi_{\mathrm{p,cap}}$, can be calculated as:

$$\phi_{\mathrm{p,cap}} = \frac{S_{\mathrm{d,p}}}{S_{\mathrm{d}}} = \frac{\int_{\vartheta_1}^{\vartheta_2} \int_{\varphi_1(\vartheta)}^{\varphi_2(\vartheta)} r_{\mathrm{d}}^2 \sin\vartheta \, \mathrm{d}\varphi \, \mathrm{d}\vartheta}{4\pi r_{\mathrm{d}}^2}, \tag{8}$$

where $S_{\mathrm{d,p}}$ is the droplet surface area covered by the particle, and S_{d} is the droplet surface area. The value of $S_{\mathrm{d,p}}$ is determined through numerical integration, with the procedure detailed in Section S1 of the Supplemental Material [61].

B. Monte Carlo method

The RSA process of particles can be simulated using the MC method. At each adsorption attempt, a particle, with a random size and at a random location constrained by the geometric relationships defined in Section II A, is generated. Its overlap with previously adsorbed particles is then examined. Based on the result, the particle is either adsorbed or discarded. This MC simulation yields the evolution of the surface coverage ϕ and the number of adsorbed particles N_{ad} as a function of the number of attempts n. The simulation procedure is detailed in the following part.

1. *Spherical particles*

This study investigates the effect of particle polydispersity on the adsorption process. The radii of a distribution of spherical particles, r_p, are assumed to follow a normal function, $\mathcal{N}(\mu, \sigma^2)$, truncated to the range $[\mu - 3\sigma, \mu + 3\sigma]$. The parameters μ and σ are equal to the mean (μ_X) and the standard deviation (σ_X) of the distribution, respectively. However, it should be emphasized that the methodology is not limited to a normal distribution, and it can be easily extended to other particle size distribution functions. Two approaches are employed to generate particle radii:

1. Infinite particle method: New radii are continuously generated from the truncated normal distribution;

2. Finite particle method: A total of N_p particle radii are first generated from the truncated normal distribution to form a finite pool. At each attempt, a particle with a specific radius is randomly selected from this pool. If the corresponding particle is successfully adsorbed, the radius is removed from the pool; otherwise, it is returned for future attempts.

In the infinite particle method, adsorption does not affect the available particles for future adsorption attempts, implying an infinite number of particles. This approach eliminates the influence of particle number and is therefore used in the investigation of other influencing factors, such as particle polydispersity and particle size. In contrast, the finite particle method accounts for a limited number of particles, as in practical applications. This method is mainly applied in the establishment of a generalized coverage evolution model.

To generate a random location for a spherical particle, a spherical coordinate system, $(\varrho, \vartheta, \varphi)$, with its origin at the droplet center, is adopted. According to the geometric relationships in Section II A 1, the effect of surface curvature is incorporated by setting $\varrho = l_\mathrm{dp}$, where l_dp is calculated using Eq. (2). Two additional random values, ϑ and φ, are then required to determine the particle's location. Since the droplet surface is continuous and all locations are equally probable, φ is drawn from a uniform distribution $\mathcal{U}[0, 2\pi]$, and ϑ is generated by sampling $\cos\vartheta \sim \mathcal{U}[-1, 1]$. This sampling method ensures uniform distribution over the spherical surface.

The overlap between two spherical particles is checked by comparing the distance between

their centers with the sum of their radii. If the center-to-center distance is less than the sum, an overlap is detected and the new particle is discarded.

2. Capsule-shaped particles

For polydisperse capsule-shaped particles, a fixed aspect ratio ϵ is specified. Two distributions are adopted for particle length, l_{p}, in this study. One is the normal distribution $\mathcal{N}(\mu,\, \sigma^2)$, truncated to the range $[\mu - 3\sigma,\, \mu + 3\sigma]$, with $\mu = \mu_{\mathrm{X}}$ and $\sigma = \sigma_{\mathrm{X}}$. The other is the lognormal distribution $\mathcal{L}(\mu,\, \sigma^2)$, truncated to the range $[\exp(\mu - 3\sigma),\, \exp(\mu + 3\sigma)]$ with $\mu = \ln\left(\mu_{\mathrm{X}}^2/\sqrt{\mu_{\mathrm{X}}^2 + \sigma_{\mathrm{X}}^2}\right)$ and $\sigma^2 = \ln\left(1 + \sigma_{\mathrm{X}}^2/\mu_{\mathrm{X}}^2\right)$. μ_{X} and σ_{X} are the mean and the standard deviation of the distributions, respectively.

As with spherical particles, two random numbers are used to determine the particle's position on the droplet surface. However, due to the anisotropic nature of capsule-shaped particles, orientation also influences the adsorption process. In our approach, the orientation is restricted to lie within the plane tangent to the spherical surface passing through the particle's center. Accordingly, an additional random angle ϖ, sampled from a uniform distribution $\mathcal{U}[0,\, 2\pi]$, is introduced to specify the particle's orientation.

To examine the overlap between two capsule-shaped particles, each is modeled as a line segment with rounded ends. The shortest distance between the segments is computed and compared with the sum of their radii [62] to determine whether an overlap occurs.

3. Additional simulation details

In this study, each simulation ran for $n = 1 \times 10^8$ adsorption attempts. This number was sufficiently large to reach a high coverage, but not enough to ensure reaching the jamming state. As mention previously, ϕ increases toward ϕ_{j} following the power law, $\phi_{\mathrm{j}} - \phi(n) \sim n^{-1/d}$. Approaching the jamming state, the number of failed attempts between two successive successful adsorption events grows rapidly, making the MC simulations computationally infeasible.

To address this problem, a voxel method for polydisperse, spherical particles is developed based on the work of Ref. [35] and Ref. [18]. In the developed method, each voxel has three dimensions: the first two discretize the droplet surface, and the third discretizes the

particle radius. The new method can efficiently obtain the jamming coverages of polydisperse spherical particles. Details of the developed voxel method are provided in Section S2 of the Supplemental Material [63]. For spherical particles, the voxel method is applied based on the results of the MC simulations to obtain the coverage and the number of adsorbed particles at the jamming state.

For capsule-shaped particles, the voxel method becomes more challenging due to the additional complexity introduced by particle anisotropy in three dimensions. Ref. [18] proposed a voxel method for a two-dimensional problem: the RSA of discorectangles (2D capsules) on a plane. However, its extension to three-dimensional particles is non-trivial. Consequently, the RSA of capsule-shaped particles is investigated using only the MC method in this study.

When the finite particle method (Section II B 1) is used, the physical time, t, can be estimated by mapping adsorption attempts to particle–emulsion droplet collisions. This mapping is necessary to study the effect of particle concentration, because expressing coverage evolution as $\phi(n)$ assumes a concentration-independent attempt rate and thus obscures the influence of particle concentration. To this end, each adsorption attempt is interpreted as a particle–emulsion droplet collision, and the corresponding time interval is computed using a collision kernel that specifies the collision frequency [4]. In principle, turbulent kernels are most appropriate, since Pickering emulsions are generally prepared in turbulent flows induced by high shear mixers [11]. However, they require empirical constants or turbulence fields, introducing uncertainty. For simplicity, we adopt the Brownian collision kernel, which depends only on material properties and temperature. Accordingly, this time mapping is intended to illustrate the effect of particle concentration on the RSA process, not to reproduce experimental time scales. Detailed equations are provided in Section S3 of the Supplemental Material [64] (see also references [65–68] therein).

To ensure statistical reliability of the MC simulations, the convergence with respect to the number of simulations, N_{sim}, is analyzed (detailed in Section S3 of the Supplemental Material [64]). Satisfactory convergence can be obtained for $N_{\mathrm{sim}} \geq 25$. Considering computational efficiency, most simulations in this study are performed with $N_{\mathrm{sim}} = 50$. However, when constructing the generalized coverage evolution model for capsuled-shaped particles in Section IV C, $N_{\mathrm{sim}} = 25$ is adopted to reduce computational costs while maintaining acceptable accuracy. Throughout this work, standard deviations are generally reported alongside mean values by error bars. However, in most cases, the deviations are too small to be visible

in the figures.

C. Generalized coverage evolution model

The coverage evolution during the RSA process can be modeled with the help of the available surface function, $ASF(\phi)$ [13, 39]. This function quantifies the probability of successful adsorption at a given surface coverage ϕ. However, the parameters of $ASF(\phi)$ may vary with influencing factors of the RSA process, such as particle polydispersity and emulsion droplet–particle size ratio. To establish a generalized coverage evolution model applicable across varied conditions, the response surface methodology is adopted to relate the influencing factors to the parameters of $ASF(\phi)$.

1. Available surface function

The coverage change rate concerning the number of adsorption attempts can be written as [39]:

$$\frac{\mathrm{d}\phi}{\mathrm{d}n} = \overline{\phi}_{\mathrm{p}}(\phi) ASF(\phi), \tag{9}$$

where $\overline{\phi}_{\mathrm{p}}(\phi)$ is the average coverage provided by a single particle at the coverage of ϕ. For polydisperse particles, $\overline{\phi}_{\mathrm{p}}(\phi)$ decreases with increasing ϕ because smaller particles more easily fill the space between previously adsorbed particles. For simplicity, a constant $\overline{\phi}_{\mathrm{p}}$ based on the mean particle size is used in this study. Then, we have:

$$ASF(\phi) = \frac{1}{\overline{\phi}_{\mathrm{p}}} \frac{\mathrm{d}\phi}{\mathrm{d}n}, \tag{10}$$

where $\mathrm{d}\phi/\mathrm{d}n$ can be obtained from the MC simulations [41].

Ref. [39] proposed two fitting expressions for $ASF(\phi)$, which cover both the low-coverage and the asymptotic behaviors, referred to here as Fit 1 and Fit 2, respectively:

$$ASF_1(x) = (1-x)^4(1 + c_1 x + c_2 x^2), \tag{11}$$

$$ASF_2(x) = \frac{(1-x)^4}{(1 + d_1 x + d_2 x^2)}, \tag{12}$$

where $x = \phi/\phi_{\mathrm{j}}$, ϕ_{j}, c_1, c_2, d_1, and d_2 are fitting parameters. Additionally, we propose a new expression (denoted as Fit 3) purely from fitting considerations as:

$$ASF_3(y) = e_1 y^{e_2(1+\exp(e_3 y))}, \tag{13}$$

where $y = \phi_{\mathrm{j}} - \phi$, ϕ_{j}, e_1, e_2, and e_3 are fitting parameters. Compared with Fit 1 and Fit 2, Fit 3 adopted a coverage-dependent exponent, which is more flexible to deal with the adsorption of polydisperse or anisotropic particles.

Once $ASF(\phi)$ is known, the coverage evolution model can be written as:

$$\phi(n + \Delta n) = \phi(n) + \overline{\phi}_{\mathrm{p}} ASF(\phi(n))\Delta n, \tag{14}$$

where $\phi(0) = 0$, and Δn is the step. Eq. (14) can be solved using a forward Euler method.

2. Response surface methodology

The response surface methodology is a statistical technique used to develop an adequate functional relationship between a response of interest, y, and a number of associated input variables denoted by x_i [69]. In this study, a second-order response surface model is adopted to link influencing factors to $ASF(\phi)$ parameters, which can be expressed as [70]:

$$y = \beta_0 + \sum_{i=1}^{N} \beta_i x_i + \sum_{i=1}^{N} \beta_{ii} x_i^2 + \sum_{i=1}^{N-1} \sum_{j=i+1}^{N} \beta_{ij} x_i x_j + \epsilon_{\mathrm{RSM}}, \tag{15}$$

where y is the response ($ASF(\phi)$ parameters), x_i are the input variables (influencing factors of the RSA process), such as particle polydispersity or emulsion droplet–particle size ratio, β_0, β_i, β_{ii}, and β_{ij} are the regression coefficients to be estimated, N is the number of input variables, and ϵ_{RSM} is a random error term with a zero mean.

To construct the generalized coverage evolution model, the Latin hypercube sampling (LHS) method [70] is employed to generate combinations of influencing factors as input conditions for the MC simulations. The resulting simulation data form the training dataset, which is first used to fit the parameters of $ASF(\phi)$ [71]. Each fitted parameter is then regressed against the training conditions to develop a generalized coverage evolution model applicable across varied conditions. To validate the constructed model, the central composite design (CCD) [70] is employed to generate a separate set of input conditions distinct from those in the training dataset. Model accuracy is evaluated using the coefficient of determination (R^2) [70] and the mean absolute percentage error (MAPE) [72]. The detailed construction procedure is provided in the Supplemental Material (Section S4 [73]).

It is important to emphasize that the generalized coverage evolution model is purely empirical. Although it does not capture the underlying physics of the RSA process, it provides

a practical approximation that describes the relationships between key influencing factors and the $ASF(\phi)$ parameters. Furthermore, the proposed framework is general and adaptable: it can be readily extended to Pickering particles with different properties by updating the MC simulation setups (i.e., the representative samples used in applying response surface methodology) and, if necessary, adjusting the fitting expression of $ASF(\phi)$.

III. ADSORPTION OF SPHERICAL PARTICLES

In this section, the RSA process of spherical Pickering particles was investigated from both the asymptotic and kinetic perspectives. The effects of key influencing factors are analyzed, and a generalized coverage evolution model is developed.

A. Infinite particles

The effects of polydispersity, emulsion droplet–particle radius ratio, and contact angle on the RSA process of Pickering particles are investigated in this work. The evolutions of the number of adsorbed particles, N_{ad}, and the coverage, ϕ, are obtained from the MC simulations. The jamming coverage, ϕ_{j}, and the free energy of particle desorption, ΔG_{d}, are obtained using the voxel method. TABLE I summarizes the setups for the simulations. The polydispersity is measured by the coefficient of variation defined as $CV = \sigma_{\mathrm{X}}/\mu_{\mathrm{X}}$. Higher CV gives a wider particle size distribution, namely, higher polydispersity.

1. Effect of polydispersity

FIG. 3 shows the effect of polydispersity on the RSA process. FIG. 3(a) and FIG. 3(b) present the variations of the jamming coverage ϕ_{j} and the normalized free energy of particle desorption $\Delta G_{\mathrm{d}}/k_{\mathrm{B}}T$ with the coefficient of variation CV. The mean values and the standard deviations are represented by circles and error bars, respectively. The small standard deviations indicate that the number of MC simulations is sufficiently large to yield reliable results. It can be observed that both ϕ_{j} and ΔG_{d} increase with CV. According to Eq. (5), the second term, $A_{\mathrm{pw}} \cos\theta$, vanishes when $\theta = 90°$. Consequently, ΔG_{d} increases proportionally with ϕ_{j}. Additionally, $\Delta G_{\mathrm{d}} \gg k_{\mathrm{B}}T$, indicating a desorption barrier far above

TABLE I. The MC simulation setups for spherical particles.

Variables[a]	Polydispersity	Radius ratio	Contact angle	Particle number[b]
μ_{X} (µm)	1	1	1	1
CV (-)	0, 0.05, 0.1, 0.2	0.1	0.1	0.1
$r_{\mathrm{d}}/r_{\mathrm{p}}$ (-)	40	20, 40, 100	40	40
θ (°)	90	90	90, 120, 150	90
$m_{\mathrm{p}}/m_{\mathrm{d}}$	∞[c]	∞	∞	0.10, 0.41, 1.63, 6.53

[a] μ_{X} is the mean particle size, $CV = \sigma_{\mathrm{X}}/\mu_{\mathrm{X}}$ is the coefficient of variation of the size distribution, r_{d} and m_{d} are the emulsion droplet radius and mass, r_{p} and m_{p} are the particle radius and mass, and θ is the contact angle.

[b] Particle number measured by the particle–emulsion droplet mass ratio $m_{\mathrm{p}}/m_{\mathrm{d}}$.

[c] $m_{\mathrm{p}}/m_{\mathrm{d}} = \infty$ represents using the infinite particle method.

thermal energy and thus confirming the high stability of Pickering emulsions.

The effect of CV can be explained by the evolution of adsorbed particle size distribution shown in FIG. 4. As adsorption proceeds, the distribution skews toward smaller sizes. At the jamming state ($n = \infty$), the share of small particles has increased significantly. This is because the small particles can further fill the space between the adsorbed large particles [30]. Increasing CV introduces particles with smaller sizes, which are further adsorbed as shown in FIG. 4(b), and cause the increment in ϕ_{j} and ΔG_{d}.

FIG. 3(c) and FIG. 3(d) present the effect of CV on the evolution of N_{ad}, and ϕ. When $n \leq 10^4$, the trends for different CV are close. At the beginning of the adsorption process, the droplet surface is empty. The probability of successful adsorption is close to 1, so N_{ad} evolutions are almost identical. The size distributions of adsorbed particles are close to the initial distributions, as shown in FIG. 4. As a result, ϕ evolutions are also close. Once the droplet has adsorbed sufficient particles, the probability of successful adsorption decreases and closely depends on the size of incoming particles. Consequently, larger CV values mean that there are smaller particles that can fill the space between the larger previously adsorbed ones. This gives a significant increment in N_{ad} when $n > 1 \times 10^4$. At the same time, ϕ increases moderately because of the smaller sizes of the newly adsorbed particles.

In addition, when the number of attempts reaches $n = 1 \times 10^8$, the coverage for $CV = 0$

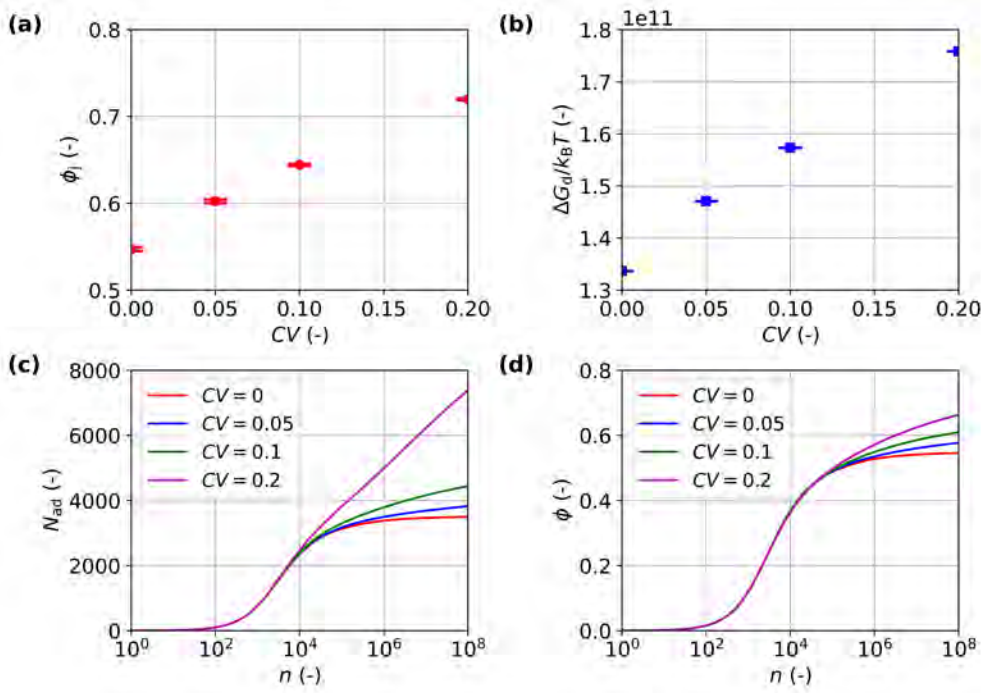

FIG. 3. The effect of polydispersity, CV, on (a) ϕ_j, (b) $\Delta G_d/k_BT$, (c) evolution of N_{ad}, and (d) evolution of ϕ.

reaches 99.6% of ϕ_j, while that for $CV = 0.2$ reaches 93.7% of ϕ_j. This indicates that 1×10^8 attempts are sufficient to approach a near-jamming state.

2. *Effect of emulsion droplet–particle radius ratio*

FIG. 5 illustrates the effect of the emulsion droplet–particle radius ratio, r_d/r_p, on the RSA process. As shown in FIG. 5(a), both the mean values and the standard deviations of ϕ_j decrease with increasing r_d/r_p. The larger variations in ϕ_j observed for smaller droplets are not caused by the limited number of simulations (see FIG. S5 in the Supplemental Material [64]) but are intrinsic to the system, reflecting a finite-size effect. When $r_d/r_p = 20$, the droplet can adsorb only a small number of particles, which is insufficient to average out the random fluctuations arising from particle size polydispersity and stochastic adsorption events. In contrast, when $r_d/r_p \geq 40$, the larger number of adsorbed particles effectively suppresses these fluctuations, resulting in smaller variations in ϕ_j.

Furthermore, it can be observed that in the production of Pickering emulsions with a sufficient quantity of particles, droplets of varying sizes tend to reach comparable levels

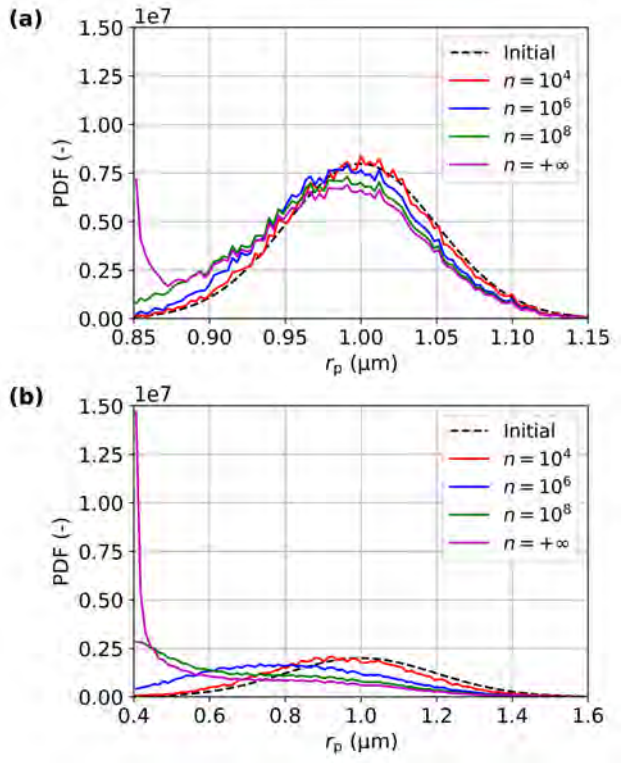

FIG. 4. Evolution of adsorbed particle size distribution of (a) $CV = 0.05$ and (b) $CV = 0.2$. n is the number of attempts. $n = \infty$ represents the jamming state obtained by the voxel method.

of coverage. This information simplifies the estimation of the API release rates because the variations in jamming coverage due to droplet polydispersity are negligible. FIG. 5(b) presents an increasing ΔG_{d}. According to Eq. (5), ΔG_{d} is proportional to r_{d}^2 when θ is 90° and ϕ_{j} is a constant.

The evolutions of N_{ad} and ϕ are shown in FIG. 5(c) and FIG. 5(d). Larger droplets ($r_{\mathrm{d}}/r_{\mathrm{p}} = 100$) adsorb more particles and have a significantly larger N_{ad}. Their coverage increases more slowly due to the large surface area. However, it finally reaches a jamming coverage close to that of smaller droplets, as mentioned previously.

3. Effect of contact angle

FIG. 6 shows the effect of contact angle, θ, on the RSA process. Both ϕ_{j} and ΔG_{d} decrease as θ increases from 90° to 150°, as shown in FIG. 6(a) and FIG. 6(b). According to Eq. (3), for a fixed $r_{\mathrm{d}}/r_{\mathrm{p}}$, β reaches its maximum value when $\theta_{\mathrm{mp}} = \arccos(r_{\mathrm{p}}/r_{\mathrm{d}})$, which corresponds to an angle smaller than 90°. β increases monotonically for $0° \leq \theta \leq \theta_{\mathrm{mp}}$,

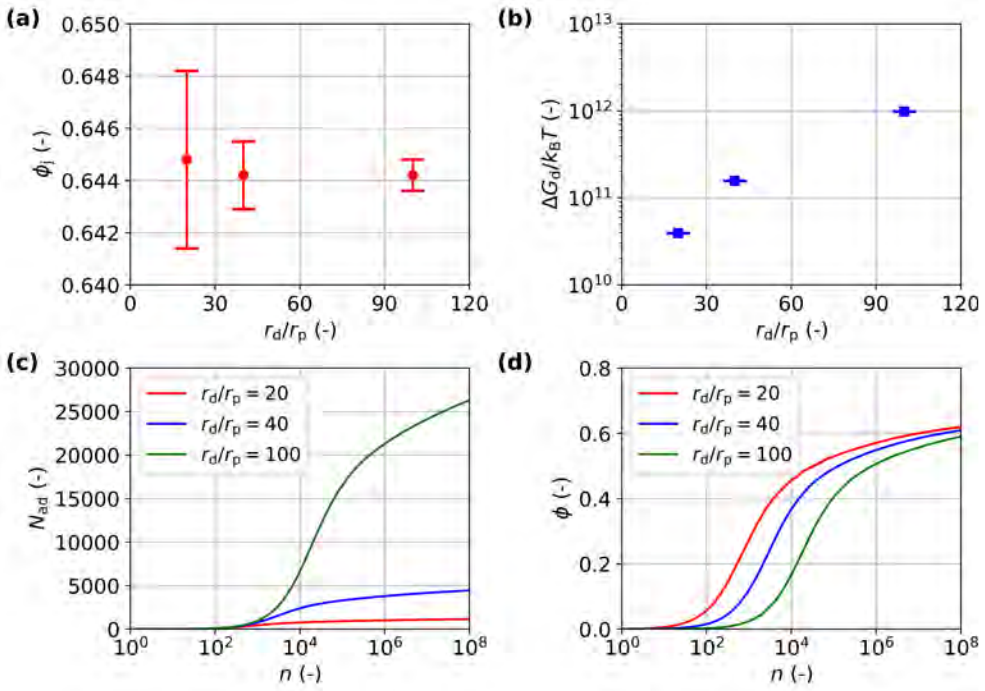

FIG. 5. The effect of emulsion droplet–particle radius ratio, r_d/r_p, on (a) ϕ_j, (b) $\Delta G_d/k_BT$, (c) evolution of N_{ad}, and (d) evolution of ϕ.

and decreases monotonically for $\theta_{mp} \leq \theta \leq 180°$. Therefore, within the considered range, [90°, 180°], the coverage provided by a single spherical particle, $\phi_{p,sph}$, decreases according to Eq. (4). Meanwhile, the emulsion droplet–particle center distance, l_{dp}, increases slightly, as given by Eq. (2). This creates additional space for particle adsorption, resulting in a modest increase in N_{ad}, as shown in FIG. 6(c). However, this slight increase in N_{ad} is insufficient to compensate for the decrease in $\phi_{p,sph}$. Consequently, ϕ_j decreases as θ increases from 90° to 150°, as illustrated in FIG. 6(d).

The decreasing trend of ΔG_d is more significant than that of ϕ_j because the second term in Eq. (5), $A_{pw}\cos\theta$, becomes negative when $\theta > 90°$. This finding supports the argument of Ref. [47] that θ should be between 30° and 150° to have a sufficient energy barrier to prevent particle desorption.

B. Finite particles

The finite particle method is employed in this section to investigate the effect of Pickering particle number and to develop a generalized coverage evolution model. The particle number

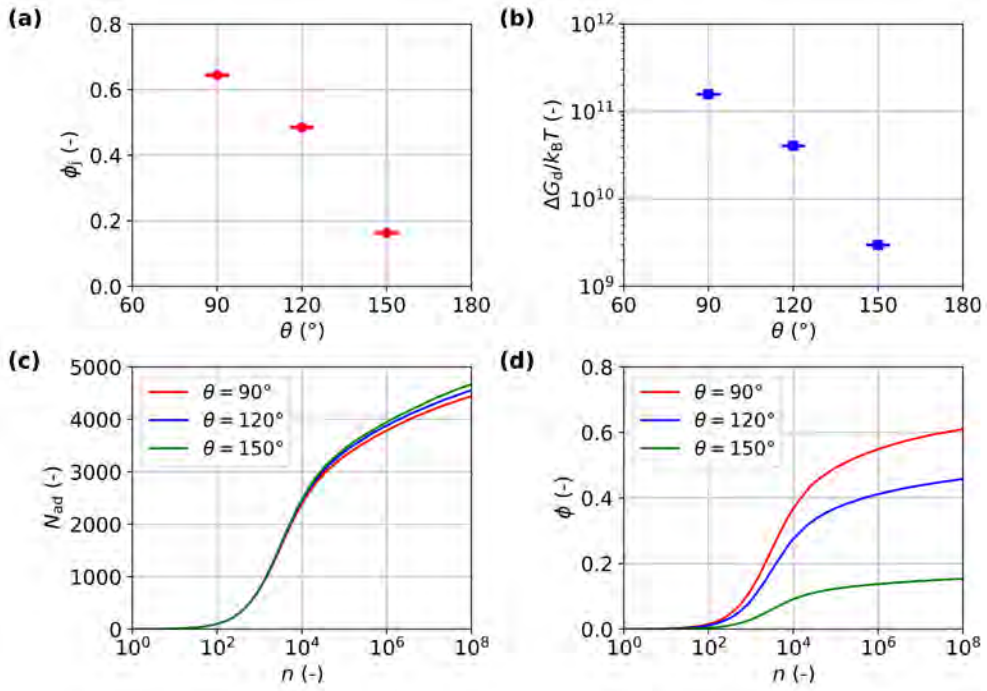

FIG. 6. The effect of contact angle, θ, on (a) ϕ_j, (b) $\Delta G_d/k_BT$, (c) evolution of N_{ad}, and (d) evolution of ϕ.

is measured by the particle–emulsion droplet mass ratio, m_p/m_d, defined as:

$$\frac{m_p}{m_d} = \frac{N_p \rho_p r_p^3}{N_d \rho_d r_d^3}, \tag{16}$$

where $N_d = 1$ is the droplet number, since we are considering the particle adsorption on one droplet. ρ_p and ρ_d are the particle and droplet density, respectively. In the case of water-in-oil emulsions stabilized by crystalline organic particles, it is reasonable to assume that $\rho_p/\rho_d = 1$ [11]. For polydisperse particles, the particle radius is calculated using the third-order moments of the normal particle size distribution $\mathcal{N}(\mu, \sigma^2)$ as $r_p^3 = \mu^3 + 3\mu\sigma^2$.

Furthermore, the Brownian collision kernel is adopted here to estimate the physical time t. The following parameters and conditions are specified: the temperature $T = 298.15$ K, the viscosity $\mu_c = 0.03$ Pa s, and the sampling volume $V = 1.34 \times 10^{-12}$ m^3 corresponding to a droplet volume fraction of 0.2 [11].

1. *Effect of finite number of particles*

FIG. 7 illustrates the effect of m_p/m_d on the RSA process (see detailed setups in TABLE I). The dashed lines represent the jamming state obtained with the assumption of an infinite number of particles ($m_p/m_d = \infty$). As m_p/m_d increases, the number of small particles increases. Both ϕ_j and ΔG_d increase accordingly and approach the case of infinite particles, as shown in FIG. 7(a) and FIG. 7(b). When $m_p/m_d = 6.53$, ϕ_j and ΔG_d are only 1% lower than the case of infinite particles.

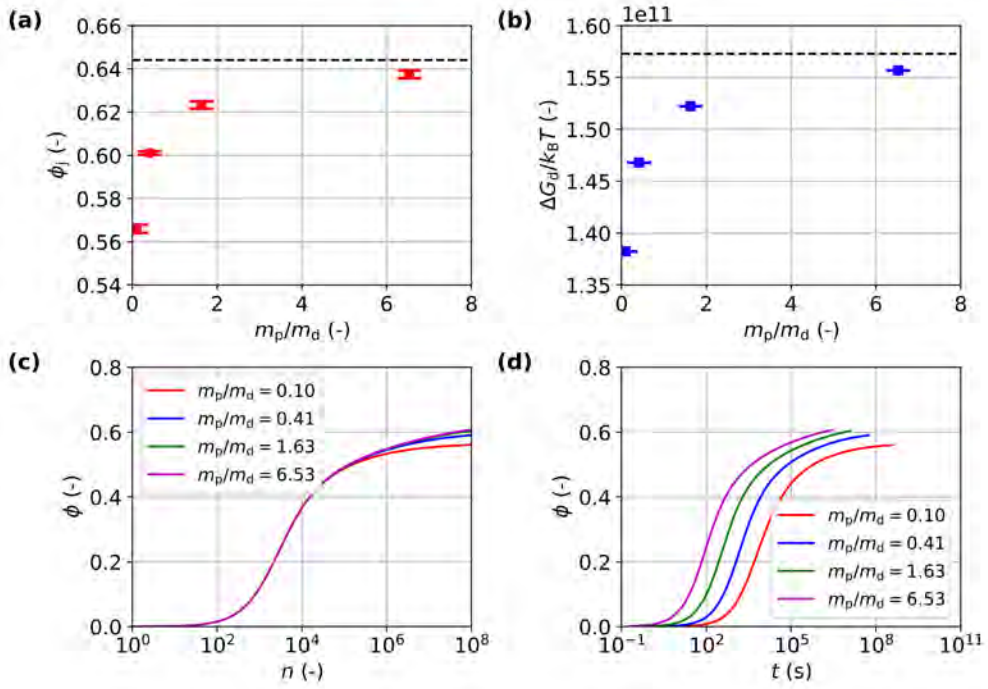

FIG. 7. The effect of emulsion droplet–particle mass ratio, m_p/m_d, on (a) ϕ_j, (b) $\Delta G_d/k_BT$, (c) ϕ evolution with the number of attempts n, and (d) ϕ evolution with physical time.

FIG. 7(c) and FIG. 7(d) show the evolution of ϕ with the number of attempts n and the physical time t, respectively. When $n \leq 1 \times 10^5$, the trends for $\phi(n)$ are almost identical. When $n > 1 \times 10^5$, the trends for $\phi(n)$ present slight differences because a larger m_p/m_d provides more small particles available for adsorption. For the temporal evolution, $\phi(t)$, a larger m_p/m_d increases the collision frequency and thus decreases the temporal interval between two attempts. Consequently, the coverage increases faster for larger values of m_p/m_d.

In addition, the Brownian kernel predicts a much slower adsorption process than that in the experiment [11], taking days to reach a moderate coverage (e.g., $\phi = 0.5$). For

Pickering emulsions prepared with high shear mixers, turbulent kernels are the appropriate choice and can reproduce experimental time scales if the turbulent flow field and empirical constants are available. However, reproducing absolute time scales is not the aim here. Our goal is to isolate how particle concentration (via $m_\mathrm{p}/m_\mathrm{d}$) affects the temporal evolution of coverage. Both Brownian and turbulent kernels yield the same relative trend, increasing $m_\mathrm{p}/m_\mathrm{d}$ accelerates coverage growth (see Fig. S3 in the Supplemental Material [64]). The Brownian kernel also avoids the need to determine turbulence fields and tune empirical constants. Therefore, we use the Brownian kernel to map n to t for trend analysis, not to reproduce absolute time scales.

FIG. 8 illustrates the size distributions of the adsorbed particles and the remaining particles at the jamming state. Increasing $m_\mathrm{p}/m_\mathrm{d}$ provides more small particles for adsorption. Consequently, the skewness towards small sizes of the size distribution of the adsorbed particles becomes significant, as shown in FIG. 8(a). The adsorption process's preference for small particles can also be observed in the size distribution of remaining not adsorbed particles, as illustrated in FIG. 8(b). When $m_\mathrm{p}/m_\mathrm{d}$ is small, for example, $m_\mathrm{p}/m_\mathrm{d} = 0.10$, the smaller particles are completely adsorbed, leading to a zero fraction for particles with $r_\mathrm{p} \leq 0.92$ µm.

2. Generalized coverage evolution model for spherical particles

As discussed in previous sections, the key factors influencing the RSA process for spherical particles with a normal size distribution are the particle size distribution polydispersity CV, the emulsion droplet–particle radius ratio $r_\mathrm{d}/r_\mathrm{p}$, and the particle–emulsion droplet mass ratio $m_\mathrm{p}/m_\mathrm{d}$. Therefore, these parameters were selected as the input variables for the second-order response surface models. Their respective selected ranges, summarized in TABLE II, were determined with reference to our previous experimental work [11].

As described in Section II C, the LHS generated 21 training conditions (S01 to S21) for the three influencing factors, and the CCD generated 8 validation conditions (ST01 to ST08). They are listed in TABLE S1 and TABLE S3 of the Supplemental Material [73], respectively. Because $ASF(\phi)$ plays an important role in the coverage evolution model, the three fitting expressions (Eq. (11) to Eq. (13)) were evaluated first. Among the parameters of $ASF(\phi)$, ϕ_j was obtained using the voxel method, while the remaining ones were fitted

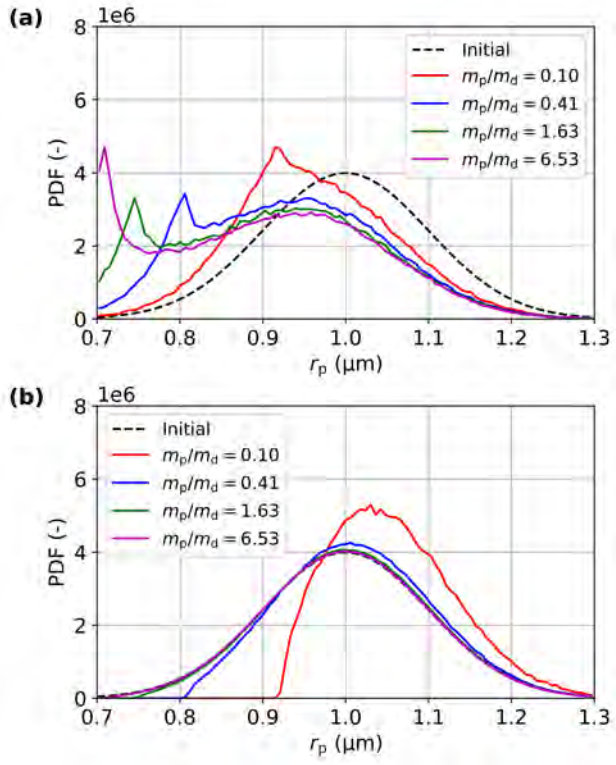

FIG. 8. The size distribution of (a) the adsorbed particles and (b) the remaining particles at the jamming state.

TABLE II. The ranges of three key influencing factors for the RSA process of polydisperse spherical particles.

Factors	Minimum	Maximum
CV (-)	0.01	0.25
r_d/r_p (-)	10	60
m_p/m_d (-)	0.10	1.63

to the training dataset. Additionally, two fitting strategies were adopted for the proposed Fit 3 to capture the asymptotic behavior better:

1. Fit 3.1: a constrain, $e_2 \geq 2$, is adopted;

2. Fit 3.2: a fixed $e_2 = 2.2682$, which is the mean of e_2 obtained by Fit 3.1, is adopted.

The performance of $ASF(\phi)$ fitting expressions was evaluated by coupling each with the coverage evolution model to predict the coverage evolution under the training conditions.

For clarity, only the case showing the largest error for Fit 3.1 (case S06 with error of 2.40%) is illustrated in FIG. 9(a). Results for the remaining cases are provided in the Supplemental Material: FIG. S7 shows coverage evolution, and TABLE S2 summarizes R^2 and MAPE [73].

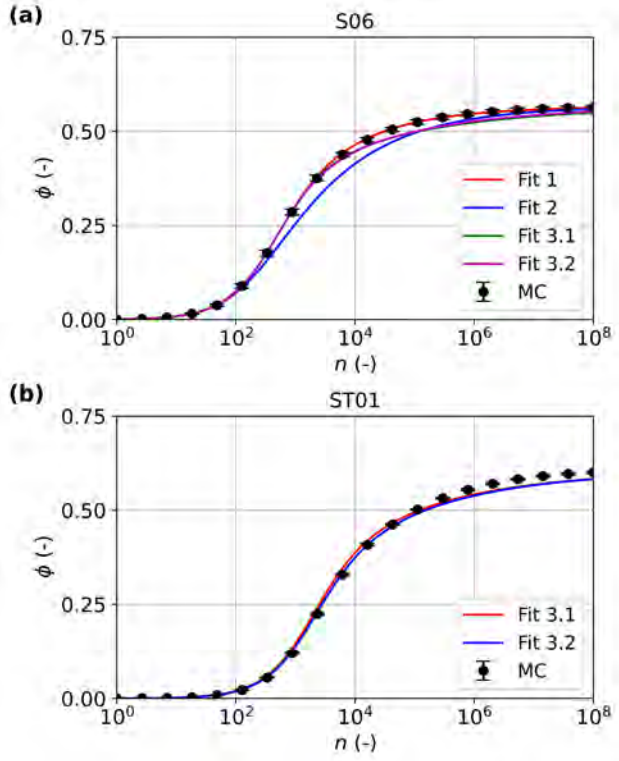

FIG. 9. Coverage evolution predicted by the coverage evolution models and MC simulations: (a) comparison of fitting expressions under the training condition, and (b) validation of the generalized coverage evolution model under the validation condition.

For polydisperse particles, the average size of adsorbed particles decreases as the jamming state is approached (see Section III A 1), producing a steeper decline in $ASF(\phi)$. Due to its coverage-dependent exponent, Fit 3 captures this behavior better than Fit 1 and Fit 2. Therefore, Fit 2 shows the poorest agreement with MC results, systematically underpredicting $ASF(\phi)$ at low coverage ($\phi \leq 0.5$), as shown in the comparison of fittings for $ASF(\phi)$ in the Supplemental Material (FIG. S6 [73]). Moreover, Fit 3.1 outperforms Fit 1 in 13 out of 21 cases (TABLE S2 [73]). Fit 3.2, fixing its parameter e_2, is comparable to Fit 3.1, outperforming Fit 3.1 in 9 out of 21 cases and matching it in 1 case. The standard deviation of e_2 from Fit 3.1 is 0.1420, indicating limited variability and justifying the use of a fixed

exponent in Fit 3.2 without significant loss in accuracy.

Therefore, the proposed Fit 3 provides the best agreement with MC simulations and is therefore adopted for estimating $ASF(\phi)$ in the generalized coverage evolution model throughout this study.

The generalized coverage evolution model was constructed by regressing the fitted $ASF(\phi)$ parameters against the training conditions. The regression R^2 and MAPE are summarized in TABLE III. For Fit 3.1, the regression poorly captures the variability of e_2, which also degrades the fits for e_1 and e_3. In contrast, fixing e_2 in Fit 3.2 remarkably improves the regressions for e_1 and e_3.

TABLE III. R^2 and MAPE of the second-order response surface models for $ASF(\phi)$ parameters in the RSA process of spherical particles.

Parameters	Fit 3.1		Fit 3.2	
	R^2	MAPE	R^2	MAPE
e_1 (-)	0.7926	3.47%	0.9532	1.00%
e_2 (-)	0.4209	3.73%	-	-
e_3 (-)	0.7603	16.00%	0.9269	5.00%
ϕ_j (-)	0.9657	0.50%	0.9657	0.50%

The generalized coverage evolution model was then validated against the validation conditions. For brevity, only case ST01 with the largest error of 2.63% for Fit 3.2 is shown in FIG. 9(b). The remaining results are provided in the Supplemental Material (FIG. S8 [73]). Both Fit 3.1 and Fit 3.2 provide good agreement with the MC simulations among all cases. Fit 3.2, having improved fitting quality for e_1 and e_2 by fixing e_2, outperforms Fit 3.1 in 6 out of the 8 cases (TABLE S3 [73]). Detailed second-order response surface equations for Fit 3.2 parameters are provided in the Supplemental Material (Eq. (S22) to Eq. (S25) [73]).

In summary, the proposed expression (Eq. (13)) provides a more accurate representation of $ASF(\phi)$ because of its coverage-dependent exponent. Based on this, the generalized coverage evolution model constructed using second-order response surface models is proven to be reliable for predicting droplet coverage evolution during the Pickering particle adsorption process.

IV. ADSORPTION OF CAPSULE-SHAPED PARTICLES

In this section, the RSA process of monodisperse and polydisperse capsule-shaped particles onto spherical droplet surfaces is investigated. The effects of particle polydispersity, aspect ratio, particle length, and particle number on the adsorption process were studied. The corresponding structures of emulsion droplets with adsorbed particles are presented. A generalized coverage evolution model to describe the adsorption for capsule-shaped particles is developed. TABLE IV summarizes the setups.

TABLE IV. The MC simulation setups for capsule-shaped particles.

Variables[a]	Monodisperse	Polydisperse ($\sim \mathcal{N}(\mu, \sigma^2)$)			
		Polydispersity	Aspect ratio	Length	Particle number[b]
r_p (µm)	1	-	-	-	-
μ_X (µm)	-	5	5	2.5, 5, 10	5
CV (-)	-	0.05, 0.1, 0.2	0.1	0.1	0.1
$m_\mathrm{p}/m_\mathrm{d}$ (-)	∞	∞	∞	∞	0.1, 0.41, 1.63
r_d (µm)	40	30	30	30	30
θ (°)	90	90	90	90	90
ϵ (-)	1.1, 2, 4, 8, 12, 16	5	2.5, 5, 10	5	5

[a] μ_X is the mean capsule particle length, $CV = \sigma_\mathrm{X}/\mu_\mathrm{X}$ is the coefficient of variation of the capsule particle length distribution, r_d and m_d are the emulsion droplet radius and mass, r_p and m_p are the capsule particle radius and mass, θ is the contact angle, and ϵ is the capsule particle aspect ratio.

[b] Particle number measured by the particle–emulsion droplet mass ratio $m_\mathrm{p}/m_\mathrm{d}$.

A. Monodisperse particles

FIG. 10 illustrates the effect of aspect ratio ϵ of monodisperse capsule-shaped particles on the evolutions of N_ad and ϕ, as well as on the particle packing pattern. As given by TABLE IV, the particle diameter d_p is fixed and particle length l_p changes with varying ϵ. The increasing ϵ leads to longer particles, which occupy larger droplet surface area and reduce N_ad significantly as shown in FIG. 10(a).

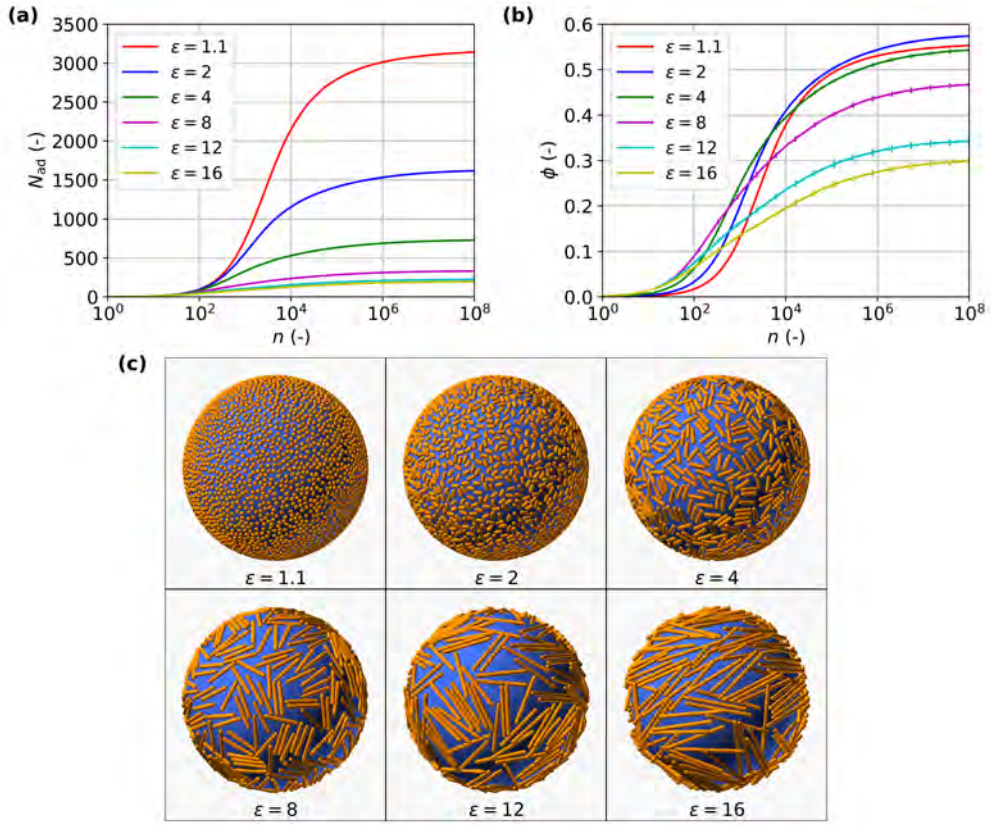

FIG. 10. The effect of aspect ratio ϵ of monodisperse capsule-shaped particles on (a) the evolution of N_{ad}, (b) the evolution of ϕ, and (c) the particle packing pattern on emulsion droplet surfaces at $n = 1 \times 10^8$.

FIG. 10(b) illustrates the evolution of ϕ. At the end of the simulation ($n = 1 \times 10^8$), $\epsilon = 2$ presents the highest coverage, and $\epsilon = 1.1$ gives the second highest coverage. Then, the coverage decreases with increasing ϵ. Similar results were found by Ref. [25], where $\epsilon = 1.46$ gave the maximum jamming coverage.

This phenomenon results from the competing effects of particle aspect ratio ϵ on single-particle coverage $\phi_{\mathrm{p,cap}}$ and exclusion zone. TABLE V gives $\phi_{\mathrm{p,cap}}$, N_{ad} and ϕ at $n = 1 \times 10^8$. Here, $\epsilon_{\mathrm{crt}} = 9.83$ is the critical aspect ratio. When $\epsilon \leq \epsilon_{\mathrm{crt}}$, the semi-spherical parts of the adsorbed particles are partially inside the droplet surface, and $\phi_{\mathrm{p,cap}}$ increases with ϵ. When $\epsilon > \epsilon_{\mathrm{crt}}$, the semi-spherical parts of the particles are completely outside the droplet surface, and $\phi_{\mathrm{p,cap}}$ remains a constant. The values of $\phi_{\mathrm{p,cap}}$ affect the exclusion zone and thus the evolution of N_{ad} and ϕ.

To illustrate the effect of ϵ, consider the cases of $\epsilon = 1.1$ and $\epsilon = 2$. When ϵ increases

from 1.1 to 2, $\phi_{\mathrm{p,cap}}$ increases by a factor of 2.02, while N_{ad} decreases by only a factor of 0.52. The product of the two factors exceeds one, indicating that the increment in $\phi_{\mathrm{p,cap}}$ outweighs the reduction in N_{ad} caused by the expanding exclusion zone. Consequently, $\epsilon = 2$ results in a higher ϕ compared to $\epsilon = 1.1$, when $n = 1 \times 10^8$.

TABLE V. The coverage of a single particle, $\phi_{\mathrm{p,cap}}$, the number of adsorbed particles, N_{ad}, and the coverage, ϕ, under different aspect ratios at $n = 1 \times 10^8$.

ϵ (-)	$\phi_{\mathrm{p,cap}}$ (-)	N_{ad} (-)	ϕ (-)
1.1	1.76×10^{-4}	3140.14 ± 13.22	0.5529 ± 0.0023
2	3.55×10^{-4}	1617.52 ± 7.87	0.5739 ± 0.0028
4	7.47×10^{-4}	726.63 ± 6.19	0.5431 ± 0.0046
8	1.41×10^{-3}	330.26 ± 3.37	0.4668 ± 0.0048
12	1.54×10^{-3}	222.48 ± 5.36	0.3424 ± 0.0083
16	1.54×10^{-3}	193.94 ± 4.99	0.2985 ± 0.0077

When $\epsilon \geq 4$, the expansion of the exclusion zone overwhelms the increment in $\phi_{\mathrm{p,cap}}$. As a result, ϕ at $n = 1 \times 10^8$ monotonically decreases with ϵ. Since these cases have reached a near jamming state, the jamming coverage ϕ_{j} obeys the above observations of ϕ at $n = 1 \times 10^8$.

Additionally, when $\epsilon \leq 8$, the increase in ϵ leads to a faster coverage change rate at the beginning of the adsorption process ($n \leq 1000$). In this condition, the probability of successful particle adsorption is high, and the evolution curves of N_{ad} are nearly identical. Consequently, particles of larger ϵ have larger $\phi_{\mathrm{p,cap}}$ and thus faster coverage change rate. This explains the experimental results of Ref. [74]. They adopted particles with aspect ratios ranging from 1 to 6 and found that increasing the aspect ratio is an efficient manner to stabilize the interface at the same low particle loading. When $\epsilon > 8$, the coverage change rate decreases with further increasing ϵ. This is caused by the constant $\phi_{\mathrm{p,cap}}$ and decreasing N_{ad}.

In summary, a higher jamming coverage ϕ_{j} or a faster coverage change rate can be obtained by adjusting the aspect ratio ϵ within a suitable range, namely, $1 < \epsilon < \epsilon_{\mathrm{crt}}$.

FIG. 10(c) illustrates the particle packing pattern on emulsion droplet surfaces with varying ϵ. As ϵ increases, the capsule-shaped particles become longer. When $\epsilon > \epsilon_{\mathrm{crt}}$, the semi-spherical parts of the particles are completely outside the droplet surface. This may

lower the stability of the Pickering emulsions. Additionally, local alignment is observed, where particles tend to align their orientations with those of nearby particles. For instance, when $\epsilon = 4$, the particles exhibit pronounced parallel alignment with their neighboring particles. This is also observed in experiments, as shown in FIG. 1.

A pair correlation function, $\eta_{\mathrm{cap}}(r)$, is adopted to measure this local alignment. Let $\mathbf{n_0}$ be the unit vector for the center line of a capsule-shaped particle, and r is the distance to its center. Within the area of $[r,\, r + \mathrm{d}r]$, there are N_r adsorbed particles. The ith particle among them has the unit vector for the center line $\mathbf{n}_{r,i}$, where $i = 1, 2, \ldots, N_r$. $\eta_{\mathrm{cap}}(r)$ is calculated as:

$$\eta_{\mathrm{cap}}(r) = \frac{\sum_{i=1}^{N_r} \arccos(\mathbf{n}_0 \cdot \mathbf{n}_{r,i})}{N_r}, \tag{17}$$

where r increases from 0 to $2r_{\mathrm{d}} = 80$ µm with $\mathrm{d}r = 0.4$ µm.

FIG. 11 shows the evolution of η_{cap} with r normalized by l_{p}. l_{p} increases with ϵ, the curves of larger ϵ ends earlier due to the upper bound of $2r_{\mathrm{d}}/l_{\mathrm{p}}$. For particles with different ϵ, η_{cap} increases from 0° to 90° as r/l_{p} increases, and the corresponding curves for different ϵ values almost coincide.

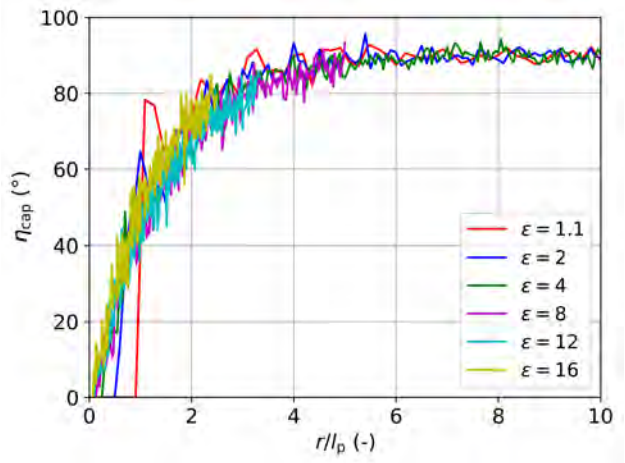

FIG. 11. The pair correlation function $\eta_{\mathrm{cap}}(r)$ of monodisperse capsule-shaped particles with different aspect ratio ϵ.

Local alignment makes a selected particle and its near neighbors, those located within a small r, closely oriented in a nearly parallel way. Therefore, η_{cap} is around zero. When $r/l_{\mathrm{p}} \geq 5$, η_{cap} reaches 90°, indicating that particles become randomly oriented and local alignment disappears. The orientation of a selected particle no longer influences those of

the particles in the area of $r/l_\mathrm{p} \geq 5$. Instead, their orientations only depend on the uniform distribution $\mathcal{U}[0,\, 2\pi]$ from which they are generated. Therefore, $\eta_\mathrm{cap}(r)$ fluctuates around 90°, which corresponds to the expected angle between two randomly oriented capsule-shaped particles.

B. Polydisperse particles

FIG. 12 shows the effect of polydispersity, aspect ratio, mean particle length, and particle–emulsion droplet mass ratio on coverage evolution and particle packing pattern obtained from the MC simulations. Similar to the case of spherical particles, increasing polydispersity (CV) of the particle size distribution introduces smaller particles that fill the spaces between previously adsorbed larger ones, as shown in FIG. 12(b). Consequently, ϕ at $n = 1 \times 10^8$ increases, as illustrated in FIG. 12(a).

FIG. 12(c) and FIG. 12(d) show the effects of aspect ratio ϵ on the coverage evolution and particle packing pattern, respectively. In this case, the particle length l_p follows a normal distribution $\mathcal{N}(\mu,\, \sigma^2)$. Increasing ϵ decreases particle diameter d_p, producing narrower particles with smaller single-particle coverage $\phi_\mathrm{p,cap}$, as shown in FIG. 12(d). Consequently, FIG. 12(c) shows that increasing ϵ slows the coverage growth.

When ϵ is fixed and the mean particle length increases, the particles become both longer and thicker (FIG. 12(f)), leading to a higher $\phi_\mathrm{p,cap}$ and a faster coverage increase (FIG. 12(e)).

Finally, FIG. 12(g) and FIG. 12(h) illustrate the effect of particle concentration, represented by $m_\mathrm{p}/m_\mathrm{d}$. Although the differences are small in FIG. 12(h), the case with $m_\mathrm{p}/m_\mathrm{d} = 1.63$ adsorbs $N_\mathrm{ad} = 1559$ particles at $n = 1 \times 10^8$, about 11.9% more than the case with $m_\mathrm{p}/m_\mathrm{d} = 0.10$, resulting in a slightly higher coverage in FIG. 12(g).

C. Generalized coverage evolution model for capsule-shaped particles

This section develops a generalized coverage evolution model for the adsorption of capsule-shaped particles with lognormal size distributions. MC simulations for the RSA process of capsule-shaped particles are more computationally intensive. Moreover, the objective of this study is to demonstrate the framework for constructing a generalized coverage evolution model using response surface methodology. Therefore, only two influencing factors, particle

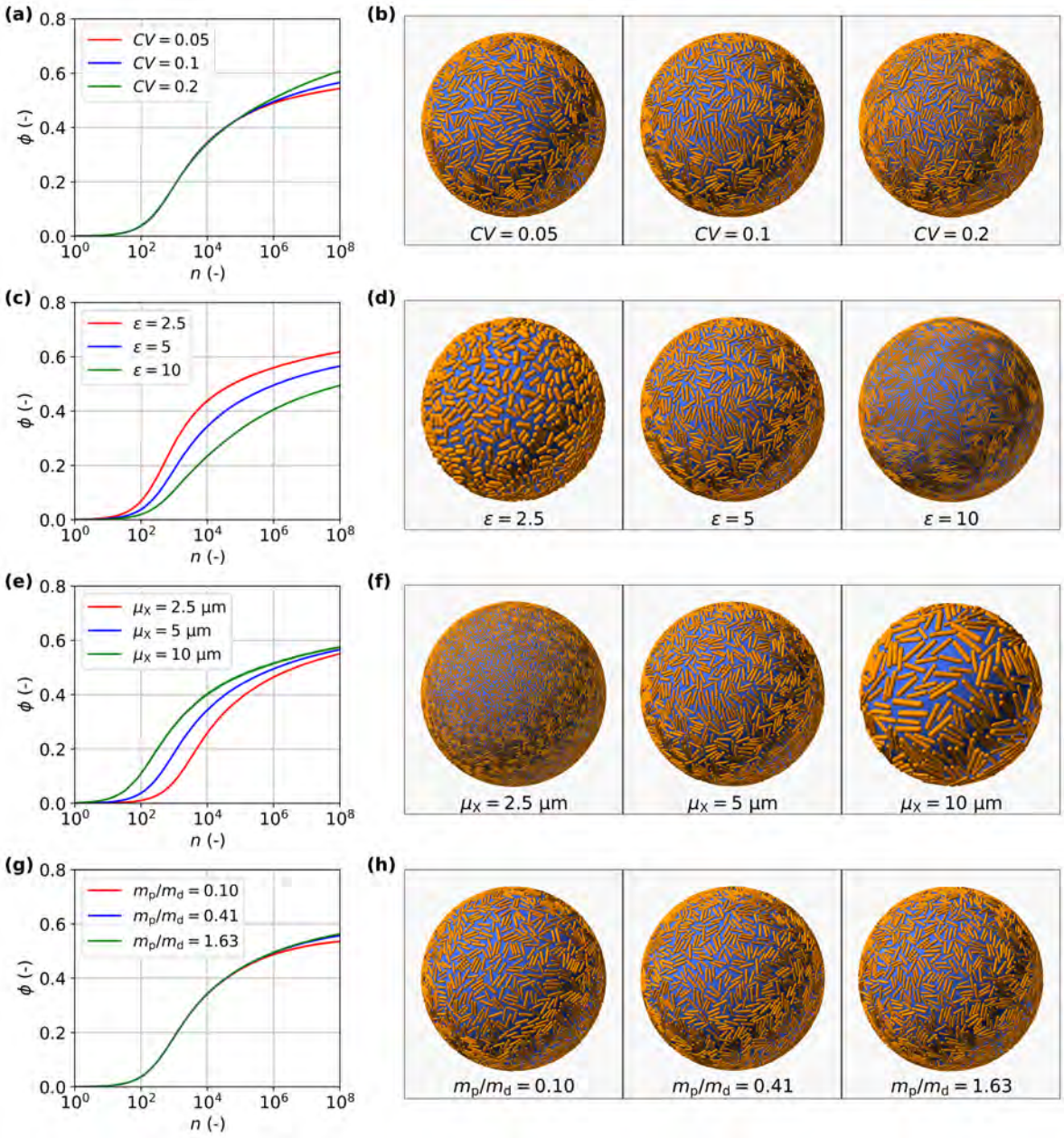

FIG. 12. The coverage evolution and particle packing pattern (at $n = 1 \times 10^8$) for polydisperse capsule-shaped particles under varying conditions: (a) and (b) for coefficient of variation CV, (c) and (d) for aspect ratio ϵ, (e) and (f) for mean particle length μ_{X}, (g) and (h) for particle–emulsion droplet mass ratio $m_{\mathrm{p}}/m_{\mathrm{d}}$.

polydispersity CV and emulsion droplet–particle size ratio $r_{\mathrm{d}}/l_{\mathrm{p}}$, were considered. Their respective ranges are summarized in TABLE VI with reference to findings of our previous works [11]. The particle–emulsion droplet mass ratio $m_{\mathrm{p}}/m_{\mathrm{d}}$ was fixed at 1, which ensures

a sufficient number of particles for the RSA process.

TABLE VI. The ranges of two key influencing factors for the RSA process of polydisperse capsule-shaped particles.

Factors	Minimum	Maximum
CV (-)	0.01	0.5
$r_\mathrm{d}/l_\mathrm{p}$ (-)	10	60

As outlined in Section II C, the LHS generated 15 training conditions (C01 to C15), and the CCD generated 6 validation conditions (CT01 to CT06). They are detailed in TABLE S4 and TABLE S6 of the Supplemental Material [73], respectively. Fit 3.1 and Fit 3.2 were used for $ASF(\phi)$ due to their good accuracy (Section III B 2). For capsule-shaped particles, the jamming coverage ϕ_j was treated as a fitted parameter, which increases the fitting complexity. To improve fitting quality, a weighted least-squares method [71] was applied by assigning higher weights to high-coverage points ($\phi \geq 0.5$) to better fit ϕ_j.

The performance of Fit 3.1 and Fit 3.2 was evaluated for capsule-shaped particles under the training conditions. Fit 3.2 fixed its parameter e_2 to 3.5747, the mean e_2 of Fit 3.1. For clarity, only case C08, the one with the largest error of 3.90% for Fit 3.1, is shown in FIG. 13(a). Results for all remaining cases are provided in the Supplemental Material: FIG. S9 for coverage evolution and TABLE S5 for R^2 and MAPE [73]. To avoid inflated MAPE values at low coverage, only data points with $\phi \geq 0.1$ are included in the calculation. This threshold is reasonable, as most of the simulated attempts occur within this coverage range.

Overall, Fit 3.1 outperforms Fit 3.2 in 8 of the 15 cases and performs equally well in one case (see TABLE S5 [73]). The slightly reduced performance of Fit 3.2 arises from the larger variability of e_2 in Fit 3.1 (standard deviation 0.7077), indicating that fixing e_2 across all cases can compromise fitting accuracy. For example, in case C08, $e_2 = 2.1388$ in Fit 3.1 deviates significantly from the fixed mean value used in Fit 3.2, leading to a less accurate prediction by the coverage evolution model.

The generalized coverage evolution was constructed by regressing the fitted $ASF(\phi)$ parameters against the training conditions, with regression R^2 and MAPE summarized in TABLE VII. Consistent with the case of spherical particles, fixing e_2 in Fit 3.2 improves the

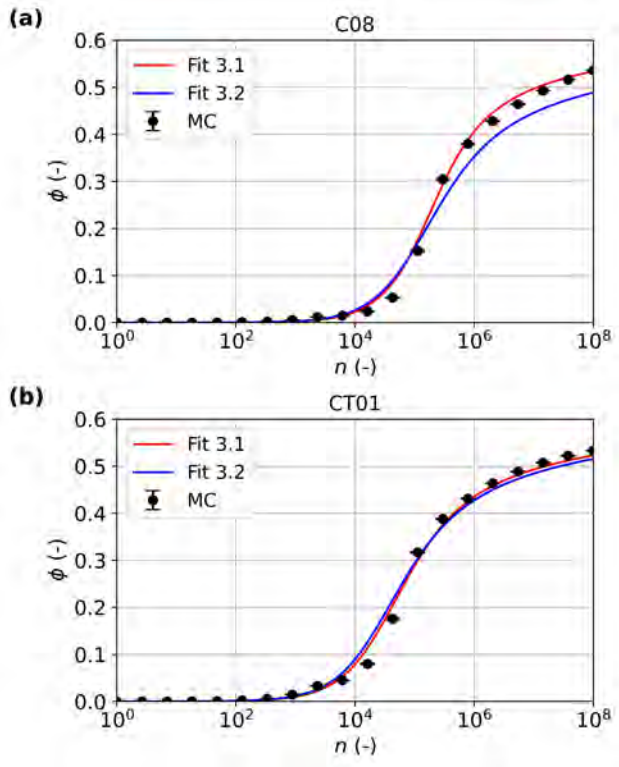

FIG. 13. Coverage evolution predicted by the coverage evolution models and MC simulations: (a) comparison of fitting expressions under the training condition, and (b) validation of the generalized coverage evolution model under the validation condition.

fitting quality for both e_1 and e_2. However, the fitting quality of all parameters in Fit 3.1 remains acceptable, indicating that it can still capture the underlying trends.

TABLE VII. R^2 and MAPE of the second-order response surface models for $ASF(\phi)$ parameters in the RSA process of capsule-shaped particles.

Parameters	Fit 3.1		Fit 3.2	
	R^2	MAPE	R^2	MAPE
e_1 (-)	0.8755	11.10%	0.9471	3.65%
e_2 (-)	0.8724	5.68%	-	-
e_3 (-)	0.7695	16.02%	0.9191	12.01%
ϕ_j (-)	0.9900	0.53%	0.9900	0.53%

Finally, the generalized coverage evolution model was validated on the validation condi-

tions. For brevity, only case CT01, the one showing the largest error of 6.58% for Fit 3.1, is shown in FIG. 13(b). The remaining results are provided in the Supplemental Material (FIG. S10 for coverage evolution and TABLE S6 for R^2 and MAPE [73]). Overall, model predictions agree well with the MC simulations. Fit 3.1, which allows e_2 to vary, outperforms Fit 3.2 in 5 of the 6 validation cases, indicating that Fit 3.1 provides a more accurate representation of $ASF(\phi)$ for polydisperse, anisotropic capsule-shaped particles. The detailed second-order response surface expressions for Fit 3.1 parameters are provided in the Supplemental Material (Eq. (S26) to Eq. (S29) [73]).

In summary, the generalized coverage evolution model based on Fit 3.1 proves effective in capturing the RSA process of capsule-shaped particles across a wide range of conditions, offering a reliable predictive framework for future applications.

V. CONCLUSIONS

Micron-sized, crystalline particles have received increasing attention for stabilizing Pickering emulsions. Due to their larger sizes, the effects of the curvature and the finite size of spherical emulsion droplet surfaces should be considered to describe interfacial adsorption. This study investigates the random sequential adsorption (RSA) of micron-sized particles onto spherical surfaces from both low-coverage and asymptotic perspectives. Isotropic spherical particles and anisotropic capsule-shaped particles were considered. A Monte Carlo (MC) method was employed to simulate the RSA process, systematically exploring the effects of several factors. A new expression of the available surface function, $ASF(\phi)$, was proposed and compared with those from the literature. Based on this, a generalized coverage evolution model was constructed by linking key influencing factors of the RSA process to $ASF(\phi)$ parameters by the response surface methodology.

The effects of curvature and finite size are incorporated by the emulsion droplet–particle geometric relationships derived from the spherical emulsion droplet surfaces. Regarding the influencing factors in the RSA process of Pickering particles, the jamming coverage, ϕ_{j}, and free energy of particle desorption, ΔG_{d}, increase with particle polydispersity due to the larger number of smaller particles. For emulsion droplets produced in the same batch, their jamming coverages are almost identical regardless of the emulsion droplet–particle size ratio. Increasing the contact angle from 90° to 150° leads to reductions in both ϕ_{j} and ΔG_{d}, which

means lower surface coverage and emulsion stability. A higher particle–emulsion droplet mass ratio increases ϕ_{j}, closer to the case of infinite particles. Meanwhile, this also increases collision frequency and accelerates the adsorption process. In particular, for capsule-shaped particles, the aspect ratio, ϵ, plays an important role. When ϵ is larger than a critical value, the semi-spherical parts of particles are outside of the droplet interfaces and provide a constant single-particle coverage due to the curvature of droplet interfaces. An aspect ratio of $\epsilon = 2$ achieves higher ϕ_{j} and faster coverage increasing rate. A local alignment, related to the long axis of capsule-shaped particles, is observed in the simulations. These findings deepen the understanding of the RSA process in Pickering emulsion production processes and provide valuable information on ϕ_{j}, which is essential to predict emulsion stability, encapsulation efficiency, and API release rate.

As for the RSA coverage evolution, a new expression for $ASF(\phi)$, with a coverage-dependent exponent, is proposed, which is more flexible and accurate than the existing expressions in the literature, using a fixed exponent. Based on this, generalized coverage evolution models are constructed for spherical and capsule-shaped particles, respectively. The key influencing factors of RSA processes are linked to the $ASF(\phi)$ parameters through second-order response surface models. The validations show that both models work well, leading to MAPE no larger than 2.63% for spherical particles and 6.58% for capsule-shaped particles in all validation cases. The generalized coverage evolution models are applicable across varied conditions and offer an efficient and practical tool to simulate the RSA behavior of Pickering particles. The presented framework for the construction of the generalized coverage evolution model can be extended to the RSA process of various kinds of Pickering emulsion formulations, prepared under various processing conditions. This is an important tool for the design and optimization of Pickering emulsion production processes, and it represents an essential step for the construction of a generalized model that describes API release from Pickering emulsion.

ACKNOWLEDGMENTS

This project has received funding from the European Research Council (ERC) under the European Union's Horizon 2020 research and innovation program (grant agreement No 949229). PI: Prof. Elena Simone. Computational resources provided by HPC@PoliTO

(www.hpc.polito.it). Prof. Marco Vanni is acknowledged for useful discussions on the sampling method of spherical surfaces and the convergence examination of the Monte Carlo method.

---

[1] C. Albert, M. Beladjine, N. Tsapis, E. Fattal, F. Agnely, and N. Huang, Pickering emulsions: Preparation processes, key parameters governing their properties and potential for pharmaceutical applications, Journal of Controlled Release **309**, 302 (2019).

[2] F. Heidari-Dalfard, S. Tavasoli, E. Assadpour, R. Miller, and S. M. Jafari, Surface modification of particles/nanoparticles to improve the stability of Pickering emulsions; a critical review, Advances in Colloid and Interface Science **336**, 103378 (2025).

[3] C. Li, Y. Li, P. Sun, and C. Yang, Pickering emulsions stabilized by native starch granules, Colloids and Surfaces A: Physicochemical and Engineering Aspects **431**, 142 (2013).

[4] G. Frungieri and H. Briesen, A population balance model for the flow-induced preparation of Pickering emulsions, Chemical Engineering Research and Design **189**, 694 (2023).

[5] B. P. Binks and T. S. Horozov, eds., *Colloidal Particles at Liquid Interfaces*, 1st ed. (Cambridge University Press, 2006).

[6] Y. Liu and Y. Xi, Colloidal systems with a short-range attraction and long-range repulsion: Phase diagrams, structures, and dynamics, Current Opinion in Colloid & Interface Science **39**, 123 (2019).

[7] J. Xu, Y. Liu, T. Guo, G. Sun, J. Luo, R. Liu, Y.-L. Steve Tse, and T. Ngai, Investigation of the Contact Angle and Packing Density of Silica Nanoparticles at a Pickering Emulsion Interface Fixed by UV Polymerization, Langmuir **38**, 4234 (2022).

[8] Y. He and X. Yu, Preparation of silica nanoparticle-armored polyaniline microspheres in a Pickering emulsion, Materials Letters **61**, 2071 (2007).

[9] H. Firoozmand and D. Rousseau, Microbial cells as colloidal particles: Pickering oil-in-water emulsions stabilized by bacteria and yeast, Food Research International **81**, 66 (2016).

[10] B. P. Binks and S. O. Lumsdon, Pickering Emulsions Stabilized by Monodisperse Latex Particles: Effects of Particle Size, Langmuir **17**, 4540 (2001).

[11] G. Del Duca, E. Parisi, F. Artusio, E. Calì, S. Fraterrigo Garofalo, C. Rosso, V. Cauda, M. R. Chierotti, and E. Simone, A crystal engineering approach for rational design of curcumin

crystals for Pickering stabilization of emulsions, Food Research International **194**, 114871 (2024).

[12] D. Ershov, J. Sprakel, J. Appel, M. A. Cohen Stuart, and J. Van Der Gucht, Capillarity-induced ordering of spherical colloids on an interface with anisotropic curvature, Proc. Natl. Acad. Sci. U.S.A. **110**, 9220 (2013).

[13] P. Kubala, P. Batys, J. Barbasz, P. Weroński, and M. Cieśla, Random sequential adsorption: An efficient tool for investigating the deposition of macromolecules and colloidal particles, Advances in Colloid and Interface Science **306**, 102692 (2022).

[14] J. Feder, Random sequential adsorption, Journal of Theoretical Biology **87**, 237 (1980).

[15] M. Cieśla and J. Barbasz, Random packing of regular polygons and star polygons on a flat two-dimensional surface, Phys. Rev. E **90**, 022402 (2014).

[16] E. L. Hinrichsen, J. Feder, and T. Jøssang, Geometry of random sequential adsorption, J Stat Phys **44**, 793 (1986).

[17] R. D. Vigil and R. M. Ziff, Random sequential adsorption of unoriented rectangles onto a plane, The Journal of Chemical Physics **91**, 2599 (1989).

[18] K. Haiduk, P. Kubala, and M. Cieśla, Saturated packings of convex anisotropic objects under random sequential adsorption protocol, Phys. Rev. E **98**, 063309 (2018).

[19] P. Abritta and R. S. Hoy, Structure of saturated random-sequential-adsorption ellipse packings, Phys. Rev. E **106**, 054604 (2022).

[20] A. Abbasi Moud, Precise Determination of the Saturation Coverage of Polygons In Silico Using Exclusion Assisted Packing Technique, J Stat Phys **190**, 93 (2023).

[21] M. Cieśla, P. Kubala, and K. Kozubek, Algorithms to generate saturated random sequential adsorption packings built of rounded polygons, Phys. Rev. E **103**, 063308 (2021).

[22] M. Cieśla, G. Pająk, and R. M. Ziff, Shapes for maximal coverage for two-dimensional random sequential adsorption, Phys. Chem. Chem. Phys. **17**, 24376 (2015).

[23] L. Petrone and M. Cieśla, Random sequential adsorption of oriented rectangles with random aspect ratio, Phys. Rev. E **104**, 034903 (2021).

[24] N. Lebovka, M. Petryk, M. O. Tatochenko, and N. V. Vygornitskii, Two-stage random sequential adsorption of discorectangles and disks on a two-dimensional surface, Phys. Rev. E **108**, 024109 (2023).

[25] N. I. Lebovka, N. V. Vygornitskii, and Y. Y. Tarasevich, Random sequential adsorption of

partially ordered discorectangles onto a continuous plane, Phys. Rev. E **102**, 022133 (2020).

[26] R. C. Doty, R. T. Bonnecaze, and B. A. Korgel, Kinetic bottleneck to the self-organization of bidisperse hard disk monolayers formed by random sequential adsorption, Phys. Rev. E **65**, 10.1103/physreve.65.061503 (2002).

[27] P. Danwanichakul and T. Charinpanitkul, Random sequential adsorption of polydisperse spherical particles: An integral-equation theory, Physica A: Statistical Mechanics and its Applications **377**, 102 (2007).

[28] N. V. Brilliantov, Yu. A. Andrienko, P. L. Krapivsky, and J. Kurths, Fractal Formation and Ordering in Random Sequential Adsorption, Phys. Rev. Lett. **76**, 4058 (1996).

[29] Z. Adamczyk, B. Siwek, M. Zembala, and P. Weroński, Influence of Polydispersity on Random Sequential Adsorption of Spherical Particles, Journal of Colloid and Interface Science **185**, 236 (1997).

[30] R. C. Hart and F. D. A. Aarão Reis, Random sequential adsorption of polydisperse mixtures on lattices, Phys. Rev. E **94**, 022802 (2016).

[31] P. Viot, G. Tarjus, S. M. Ricci, and J. Talbot, Random sequential adsorption of anisotropic particles. I. Jamming limit and asymptotic behavior, The Journal of Chemical Physics **97**, 5212 (1992).

[32] G. Zhang and S. Torquato, Precise algorithm to generate random sequential addition of hard hyperspheres at saturation, Phys. Rev. E **88**, 053312 (2013).

[33] J.-S. Wang, A fast algorithm for random sequential adsorption of discs, Int. J. Mod. Phys. C **05**, 707 (1994).

[34] G. Zhang, Precise algorithm to generate random sequential adsorption of hard polygons at saturation, Phys. Rev. E **97**, 043311 (2018).

[35] W. Kasperek, P. Kubala, and M. Cieśla, Random sequential adsorption of unoriented rectangles at saturation, Phys. Rev. E **98**, 063310 (2018).

[36] P. Schaaf and J. Talbot, Kinetics of Random Sequential Adsorption, Physical Review Letters **62**, 175 (1989).

[37] J. W. Evans, Comment on "Kinetics of random sequential adsorption", Physical Review Letters **62**, 2642 (1989).

[38] J. W. Evans, Random and cooperative sequential adsorption, Rev. Mod. Phys. **65**, 1281 (1993).

[39] S. M. Ricci, J. Talbot, G. Tarjus, and P. Viot, Random sequential adsorption of anisotropic

particles. II. Low coverage kinetics, The Journal of Chemical Physics **97**, 5219 (1992).

[40] M. Cieśla and J. Barbasz, Modelling of interacting dimer adsorption, Surface Science **612**, 24 (2013).

[41] V. Tartaglione, C. Farges, and J. Sabatier, Nonlinear dynamical modeling of adsorption and desorption processes with power-law kinetics: Application to CO 2 capture, Phys. Rev. E **102**, 052102 (2020).

[42] Z. Adamczyk, B. Senger, J.-C. Voegel, and P. Schaaf, Irreversible adsorption/deposition kinetics: A generalized approach, The Journal of Chemical Physics **110**, 3118 (1999).

[43] R. Kopelman, Fractal Reaction Kinetics, Science **241**, 1620 (1988).

[44] Y. Ho and G. Mckay, The kinetics of sorption of divalent metal ions onto sphagnum moss peat, Water Research **34**, 735 (2000).

[45] F. Brouers and O. Sotolongo-Costa, Generalized fractal kinetics in complex systems (application to biophysics and biotechnology), Physica A: Statistical Mechanics and its Applications **368**, 165 (2006).

[46] I. Tavernier, W. Wijaya, P. Van Der Meeren, K. Dewettinck, and A. R. Patel, Food-grade particles for emulsion stabilization, Trends in Food Science & Technology **50**, 159 (2016).

[47] J. Xiao, Y. Li, and Q. Huang, Recent advances on food-grade particles stabilized Pickering emulsions: Fabrication, characterization and research trends, Trends in Food Science & Technology **55**, 48 (2016).

[48] B. S. Murray, K. Durga, A. Yusoff, and S. D. Stoyanov, Stabilization of foams and emulsions by mixtures of surface active food-grade particles and proteins, Food Hydrocolloids **25**, 627 (2011).

[49] S. B. Haaj, W. Thielemans, A. Magnin, and S. Boufi, Starch Nanocrystal Stabilized Pickering Emulsion Polymerization for Nanocomposites with Improved Performance, ACS Appl. Mater. Interfaces **6**, 8263 (2014).

[50] H.-N. Liang and C.-h. Tang, Pea protein exhibits a novel Pickering stabilization for oil-in-water emulsions at pH 3.0, LWT - Food Science and Technology **58**, 463 (2014).

[51] J. Wu, M. Shi, W. Li, L. Zhao, Z. Wang, X. Yan, W. Norde, and Y. Li, Pickering emulsions stabilized by whey protein nanoparticles prepared by thermal cross-linking, Colloids and Surfaces B: Biointerfaces **127**, 96 (2015).

[52] X. Song, Y. Pei, M. Qiao, F. Ma, H. Ren, and Q. Zhao, Preparation and characterizations

of Pickering emulsions stabilized by hydrophobic starch particles, Food Hydrocolloids **45**, 256 (2015).

[53] L. A. Rosen, N. A. Seaton, and E. D. Glandt, Random sequential adsorption onto the surface of small spheres, The Journal of Chemical Physics **85**, 7359 (1986).

[54] E. R. Chen and M. Holmes-Cerfon, Random Sequential Adsorption of Discs on Surfaces of Constant Curvature: Plane, Sphere, Hyperboloid, and Projective Plane, J Nonlinear Sci **27**, 1743 (2017).

[55] B. M. Manzi, M. Werner, E. P. Ivanova, R. J. Crawford, and V. A. Baulin, Simulations of Protein Adsorption on Nanostructured Surfaces, Sci Rep **9**, 4694 (2019).

[56] P. Kubala and M. Cieśla, The effect of substrate waviness on random sequential adsorption packing properties, J. Stat. Mech. **2022**, 033303 (2022).

[57] S. Levine and B. Bowen, Capillary interaction of spherical particles adsorbed on the surface of an oil/water droplet stabilized by the particles. Part I, Colloids and Surfaces **59**, 377 (1991).

[58] R. Aveyard, J. H. Clint, and T. S. Horozov, Aspects of the stabilisation of emulsions by solid particles: Effects of line tension and monolayer curvature energy, Phys. Chem. Chem. Phys. **5**, 2398 (2003).

[59] J. C. Loudet, A. M. Alsayed, J. Zhang, and A. G. Yodh, Capillary Interactions Between Anisotropic Colloidal Particles, Phys. Rev. Lett. **94**, 018301 (2005).

[60] J. C. Loudet, A. G. Yodh, and B. Pouligny, Wetting and Contact Lines of Micrometer-Sized Ellipsoids, Phys. Rev. Lett. **97**, 018304 (2006).

[61] (2025), See Supplemental Material at URL for Section S1, which shows the calculation of the coverage of a single capsule-shaped particle.

[62] C. Ericson, *Real-Time Collision Detection*, nachdr. ed., Morgan Kaufmann Series in Interactive 3D Technology (Elsevier, Amsterdam Heidelberg, 2004).

[63] (2025), See Supplemental Material at URL for Section S2, which presents the voxel method for polydisperse spherical particles.

[64] (2025), See Supplemental Material at URL for Section S3, which shows the convergence examination for the Monte Carlo simulation.

[65] C. Coulaloglou and L. Tavlarides, Description of interaction processes in agitated liquid-liquid dispersions, Chemical Engineering Science **32**, 1289 (1977).

[66] J. Zhang, S. Xu, and W. Li, High shear mixers: A review of typical applications and studies

on power draw, flow pattern, energy dissipation and transfer properties, Chemical Engineering and Processing: Process Intensification **57–58**, 25 (2012).

[67] S. Castellano, N. Sheibat-Othman, D. Marchisio, A. Buffo, and S. Charton, Description of droplet coalescence and breakup in emulsions through a homogeneous population balance model, Chemical Engineering Journal **354**, 1197 (2018).

[68] M. J. Prince and H. W. Blanch, Bubble coalescence and break-up in air-sparged bubble columns, AIChE Journal **36**, 1485 (1990).

[69] A. I. Khuri and S. Mukhopadhyay, Response surface methodology, WIREs Comp Stat **2**, 128 (2010).

[70] R. H. Myers, D. C. Montgomery, and C. M. Anderson-Cook, *Response Surface Methodology: Process and Product Optimization Using Designed Experiments*, fourth edition ed., Wiley Series in Probability and Statistics (Wiley, Hoboken, New Jersey, 2016).

[71] W. H. Press, S. A. Teukolsky, W. T. Vetterling, and B. P. Flannery, *Numerical Recipes: The Art of Scientific Computing*, 3rd ed. (Cambridge University Press, Cambridge, 2007).

[72] A. De Myttenaere, B. Golden, B. Le Grand, and F. Rossi, Mean Absolute Percentage Error for regression models, Neurocomputing **192**, 38 (2016).

[73] (2025), See Supplemental Material at URL for Section S4, which provides the details for constructing the generalzied kinetic model for spherical and capsule-shaped particles.

[74] B. Madivala, S. Vandebril, J. Fransaer, and J. Vermant, Exploiting particle shape in solid stabilized emulsions, Soft Matter **5**, 1717 (2009).